Building and Environment 247 (2024) 111050

Contents lists available at ScienceDirect

Building and Environment

journal homepage: www.elsevier.com/locate/buildenv

Correlations among high-order statistics and low-occurrence wind speeds within a simplified urban canopy based on particle image velocimetry datasets

Fei Li [a], Chiyoko Hirose [b], Wei Wang [b], Chun-Ho Liu [a], Naoki Ikegaya [b,*]

[a] Faculty of Engineering, The University of Hong Kong, China
[b] Faculty of Engineering Sciences, Kyushu University, Japan

ARTICLE INFO

Keywords:
Urban canopy
Low-occurrence wind speed
Particle image velocimetry
High-order statistics
Probability density

ABSTRACT

Predicting infrequent and extreme wind speeds in a built environment is essential for ensuring comfortable and safe pedestrian spaces. Recent studies have employed statistical methods that assume a distribution function for wind speeds at pedestrian levels. Fundamental studies on the relationship between canopy flow and statistics are required to further develop statistical models. Therefore, this study aimed to understand the characteristics of strong and weak wind events within a simplified urban canopy and to scrutinize the relationship between high-order moments and extreme wind events. Particle image velocimetry (PIV) was employed to capture the velocities within a canopy consisting of cubes arranged in a staggered layout with a packing density of 25 %. The probability density functions (PDFs) of the velocity components classified by the mean flow patterns revealed that the PDF shapes were altered by the reverse and spanwise flows. In addition, strong correlations were verified between the gust or peak factor (PF) and high-order moments such as skewness, kurtosis, fifth-order, and sixth-order moments. Accordingly, the PF of the velocity components and wind speed were compared with the predictions by statistical methods based on the Weibull and Gram–Charlier series (GCS). These observations validate the previous statistical methods based on Weibull or GCS distributions. Although the physical interpretation of these statistics is ambiguous, the present analyses indicate that PF can be predicted by high-order moments, especially in particular, by skewness and kurtosis.

1. Introduction

An accurate prediction and suitable evaluation of pedestrian-level wind have been research targets for safe and comfortable environments within urban spaces. The rare and strong wind speeds caused by high-rise buildings have been the main interest of studies pursuing a safe outdoor environment [1]. Meanwhile, weak wind speeds have also been studied as a key factor for heat and pollutant accumulation within urban areas to evaluate the urban ventilation performance [2,3]. For both the research scopes, the urban morphology is the most influential factor for pedestrian-level winds because of the complexity of urban geometries, which mainly comprise various buildings.

With regard to the relationship between urban geometries and mean wind speeds for an effective and straightforward evaluation of urban ventilation performance, studies in recent decades have attained a consensus on the effect of urban geometry. That is, pedestrian-level wind speeds monotonically decrease with the building density (e.g. Refs. [4–7]). However, high-rise buildings can introduce fresh air into the pedestrian level, thereby increasing the pedestrian-level wind speeds [4,5]. Although further studies refined the concept with regard to how precisely various urban geometries can affect the pedestrian-level wind [8], how the mean wind speed can be formulated using geometrical parameters [7–9], and what physical quantities could be suitable for evaluating urban ventilation [10], the fundamental aspects of the geometrical effect on the mean pedestrian-level winds are well understood.

In contrast, the effects of geometry on low-occurrence wind speeds have not been understood clearly. Therefore, recent studies emphasized the importance of the stochastic characteristic of turbulent flows at the pedestrian level using computational fluid dynamics (CFD) based on unsteady simulations. For example, Ikegaya et al. [11,12] performed large-eddy simulations (LESs) of airflow around an isolated building and

* Corresponding author. Kasuga-koen 6-1, Kasuga-shi, Fukuoka, 816-8580, Japan.
E-mail address: ikegaya.naoki@kyudai.jp (N. Ikegaya).

https://doi.org/10.1016/j.buildenv.2023.111050
Received 27 June 2023; Received in revised form 14 November 2023; Accepted 15 November 2023
Available online 19 November 2023

block arrays to determine the probability density functions (PDFs) of the velocity components and wind speed. They demonstrated that the extremely strong wind speeds, represented by percentiles, are approximately proportional to the mean wind speeds. In addition, the occurrence frequencies of extremely low wind speeds monotonically decrease with the mean wind speeds and building packing density. Although these are qualitatively anticipated results, employing probabilistic information was introduced as a new approach to evaluating pedestrian-level winds. Kawaminami et al. [13] expanded their study to correlate the PDFs between wind speeds and scalar concentrations. They demonstrated that extreme scalar concentrations decrease with an increase in the mean and strong wind speeds. The results support the concept of urban ventilation enhancement by increasing the pedestrian-level winds in terms of extreme and mean concentrations. Hertwig et al. [14] conducted LESs for realistic buildings in Germany. They proposed a numerical validation procedure for turbulent flow structures around building arrays by comparing data obtained from wind-tunnel experiments (WTEs). Moreover, they validated the use of LESs to reproduce PDFs, power spectral densities (PSDs), and extreme wind events based on quadrant analysis. In addition, they demonstrated that the PDFs in certain measurement locations became more leptokurtic in both CFDs and WTEs because of the effects of buildings.

In addition, WTEs were employed to scrutinize the stochastic characteristic of the turbulent flow around buildings for pedestrian-level wind evaluation. For example, Tominaga and Shirzadi [15,16] quantified the effects of a high-rise building on the pedestrian-level wind in the canopy of a generic block array. The studies demonstrated that the PDFs were altered by the presence of a high-rise building. It is noteworthy that the high-rise building mostly reduced the streamwise velocity component, whereas it increased the spanwise velocity component. This occurred probably because of the strong downwash flow along the high-rise building. In addition, they determined the regression curve of the gust factor (GF) as a function of the mean wind speed. H'ng et al. [17] also reported the PDFs near the canopy height of realistic buildings on an urban campus in Malaysia. They demonstrated that the shapes of the PDFs could be classified by the mean wind speed. Accordingly, Hirose et al. [18] conducted WTEs using particle image velocimetry (PIV) to quantify the instantaneous velocity distribution within the canopy layer of a generic block array by developing a laser-camera system to insert a laser sheet within the canopy surrounded by blocks. This demonstrated that the GFs and peak factors (PFs) have spatial distributions within the canopy because of the surrounding buildings. Tolias et al. [19] showed that a complex building morphology causes the PDFs of the velocity components within a street canyon being a bi-modal shapes using WTE and LES. To summarize, these studies emphasized the importance of considering the stochastic characteristic of pedestrian-level wind s for a better prediction of the wind environment within urban areas.

To incorporate the statistical characteristic of the turbulent flows within urban areas, recent studies focused on developing stochastic prediction methods for low-occurrence wind speeds. Efthimiou et al. [20] proposed a statistical model for predicting extreme values based on the beta distribution of datasets from WTE, CFD, and field measurements. The statistical model can predict extreme values using a few statistics such as the mean, turbulence intensity, and integral time scale. Wang and Okaze [21,22] recently proposed a prediction method for percentile wind speeds assuming a Weibull distribution for the wind speeds around an isolated block and generic block array. They effectively adopted the mathematical characteristic of the Weibull distribution, in which the coefficient of variation, skewness s_k, GF, and PF are determined only by the shape parameter in the Weibull distribution. Hence, statistical models were formulated to predict the GF from the coefficient of variation, and the PF from s_k. The results showed that the statistical model using s_k could estimate low-occurrence wind speeds of the top 0.1 % of occurrence frequency. The deviation from the values determined by the LESs was less than 10 %. Accordingly, Wang et al. [23] and Seta et al. [24] employed a modified Gaussian distribution to describe the PDFs of velocity components and wind speeds around an isolated block and block arrays. The modified model was derived based on the Gram–Charlier series (GCS) of the Gaussian distribution. It employs the orthogonal decomposition of the PDFs using the derivatives of the Gaussian function as the basis (e.g. Ref. [25]). The coefficients in the series expansion are described by the high-order moments of the velocity components or wind speeds. Because the GCS model is expressed by a series expansion of an infinite basis, Wang et al. [23] and Seta et al. [24] quantified the prediction accuracy of the extreme values of the velocity components and wind speeds using second-to sixth-order GCS models. Wang et al. [26] expanded their previous study by comparing statistical models using the Weibull distribution and GCS models. They demonstrated that the statistical model based on the Weibull distribution can predict the percentiles with the highest accuracy, although higher-order GCS models can generally improve the prediction accuracy notwithstanding extreme outliers. Zainol et al. [27] extended the application of the GCS model to an ideal approaching flow generated by a barrier and spires in a wind tunnel to demonstrate that the model can describe the characteristic PDFs of a turbulent approaching flow. Although these statistical models cannot be applied for bi-modal PDFs, which were also observed in complex building canyons as reported by Tolias et al. [19], these studies enhance the importance of development of the statistical model for the extreme wind speed.

Although the statistical characteristic of pedestrian-level winds has been studied recently, there are still remaining questions to establish prediction procedure of the low-occurrence wind speeds at a pedestrian height. First, most previous studies have been based on CFD datasets because of the limited number of WTE datasets within canopy layers and around buildings. Accordingly, statistical models have been developed based on these CFD-based analyses. Although the validity of recent high-resolution LESs is sufficient, the validation of such unsteady simulations is still based on fundamental statistics such as the mean and standard deviations of the velocity components. Therefore, it is required to verify the relationship between the GF, PF, and other statistics observed in previous numerical studies [21–24, 26] to understand the characteristics of the infrequent wind within the canopy layer and generalize the validity of the statistical methods. Second, it is required to highlight the importance of WTE datasets and introduce a good practice of using instantaneous experimental datasets. Recently, Hirose et al. [18] proposed a novel approach to capture the velocity fields within the canopy of a simplified block array using PIV by following the similar setups to those of Ikegaya et al. [28]. They successfully demonstrated the instantaneous characteristics of canopy airflow and the spatial distributions of the GF and PF. Beyond the validations of the CFD using WTE datasets, it is demanded how we can employ the temporally and spatially high-resolution experimental data for understand the strong wind speed phenomena within the canopy layer.

This study aims to understand the characteristics of strong wind events within a canopy layer, clarify how strong wind speeds are determined, understand the spatial distribution of statistics, and scrutinize the relationship between high-order statistics and infrequent strong/weak winds. Based on these analyses, this study contributes to the generalization of prediction methods for strong wind speeds and substantiates the applicability of previous practical models such as the GCS and Weibull models to determine why these models can predict strong wind speeds. Section 2 describes the experimental methodology. In Sections 3 and 4, the results of various turbulence statistics and their relationships are discussed. Finally, Section 5 concludes the study.

2. Methodology

2.1. Wind tunnel experiment

The measurements were conducted in a closed-circuit wind tunnel located in the laboratory of the Interdisciplinary Graduate School of

Engineering Sciences, Kyushu University, Japan [28,29].

The test-section size of the wind tunnel facility has a length, width, and height of 5 m, 1.5 m, and 1.0 m, respectively. The velocity components along the streamwise x-, spanwise y-, and vertical z-directions are denoted as u, v, and w, respectively. Solid cubes with a side length of 0.1 m ($= H$) were arranged in 33 and 14 rows with a staggered distribution in the streamwise and spanwise directions, respectively (Fig. 1 (a, b)). A $27H$ fetch length was reserved upstream to develop a sufficient turbulence. The packing density of the cubes was 25 %. The target areas surrounded by cube as shown in Fig. 1. (c) and (d) were located at the center of the spanwise direction and $27H$ downstream from the edge of the upstream fetch area. The target area included three continuous horizontal square regions with a side length of 0.1 m at a particular elevation. The three zones along the flow direction were denoted as A1, A2, and A3. Three elevations, $0.1H$, $0.25H$, and $0.5H$, were selected to investigate the flow characteristics within the urban canopy. A particle image velocimetry (PIV) system consisting of a high-speed camera and laser device was placed under the wind tunnel to measure the wind field of the target area. Two trials were performed for each measurement area.

The reference wind speed u_{ref} at $z = 5H$ was measured using a static pitot tube during the PIV measurements. In 24 trials, the average reference wind speed was 5.45 m/s with a variation coefficient of 4 %. Consequently, the Reynolds number at the building height ($Re_H = u_{ref}H/\nu$) was approximately 3.6×10^4 ($\nu = 1.5 \times 10^{-5}$ m^2/s), and the order of the roughness Reynolds number ($Re^* = u^* z_0/\nu$) was 10^2 (The friction velocity is approximately 0.31 [m/s] based on the drag coefficient in Ikegaya et al. [28], and z_o is approximated as $0.1H$). This indicated that the wind field was independent of the Reynolds number above and within the canopy layer [2,30]. The boundary layer depth based on the 99 % thickness is approximately $\delta = 4H$. Fig. 2 shows the vertical profiles of the mean wind speed and standard deviation measured by a I-type hot-wire anemometer adopted from Hirose et al. [18]. Although the boundary layer depth is shallow because the fetch length is only $55H$ to keep the sufficient space for the measurement areas. Since our interest is the turbulent features within the canopy layer, the important aspect is whether the flow near the canopy elements holds the turbulence generated by the cubical roughness. Ikegaya et al. [28] employed the similar block arrays with a fetch with a $50H$ length and reported the

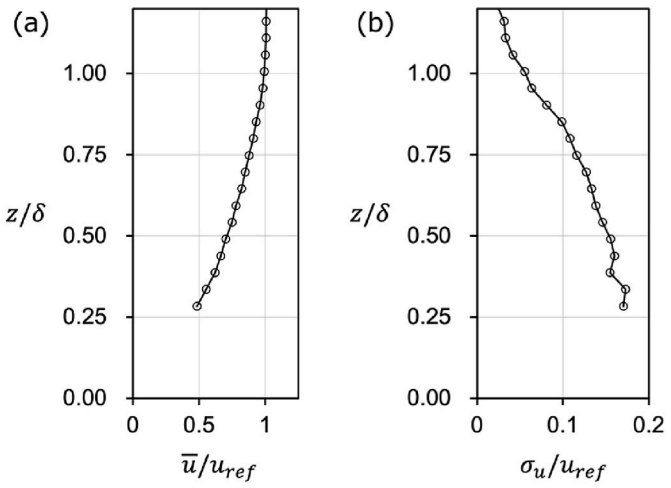

Fig. 2. Vertical profiles of (a) mean wind speed and (b) standard deviation measured by a hot-wire anemometer. The vertical axis is normalized by the boundary layer height $\delta = 4H$ based on the 99 % thickness. The data were adopted from Hirose et al. (2022) [18] and modified.

turbulent statistics measured by a X-type hot wire. According to their data, the ratios between the standard deviation for streamwise and vertical directions, σ_u, σ_w, and the friction velocity, u_*, were $\sigma_u/u_* \sim 1.9$, $\sigma_w/u_* \sim 1.4$, and $\sigma_u/\sigma_w \sim 1.3$. These values are consistent with those of the near-canopy height reported in previous studies [31].

Owing to the technical difficulties of camera installation and effective introduction of a laser sheet on the target plane, the conventional PIV system is not fully applicable for measuring the flow field within a canopy layer in wind tunnel experiments. To address this problem, a laser-camera system was designed to capture the velocity field within the canopy layer. A detailed scheme of the newly designed laser-camera system has been described [18,28]. In the wind tunnel, the PIV system was arranged appropriately to obtain the flow fields within the urban-like array (Fig. 1 (e)).

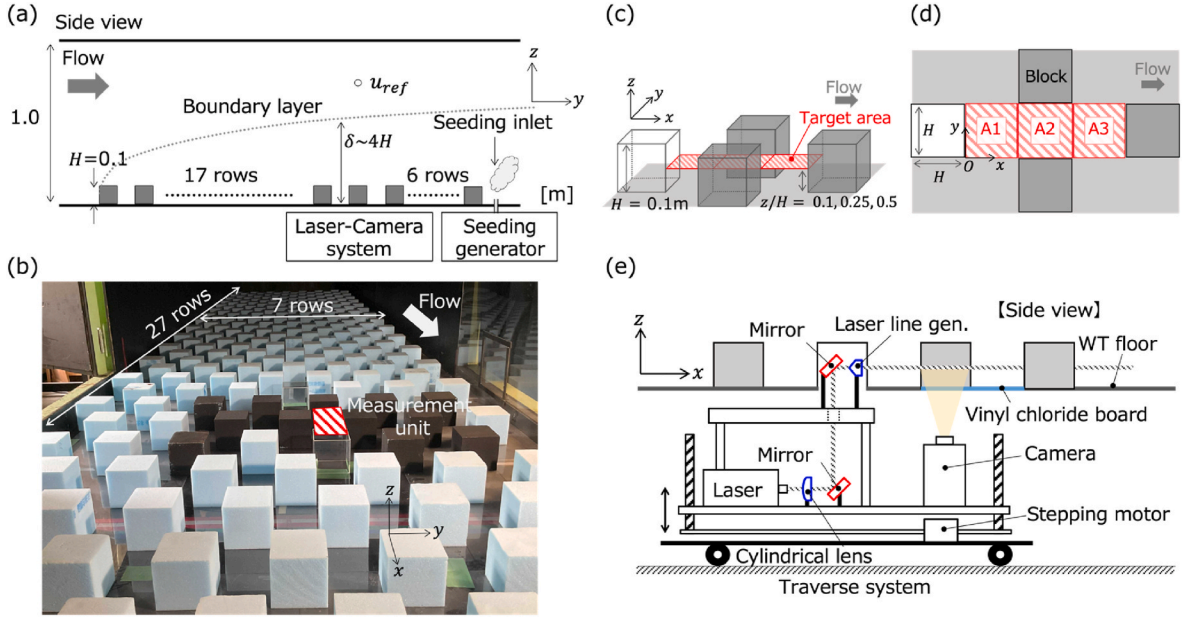

Fig. 1. (a) Schematics of the block array arrangement, (b) photo of the block array, and schematics of (c) the block arrangement, (d) measurement areas, and (e) laser-optics and camera system for the canopy flow measurements (Reprinted from Hirose et al. [18]).

2.2. PIV setting and data acquisition

During the experiment, images with particle reflection were captured in each 0.1×0.1 m^2 target area at a resolution of 1024×1024 pixels. This resulted in an image resolution of $0.099 - 0.11$ mm/pixel. A high-speed camera was used with a frame rate of 2000 fps and an exposure period of 500 μs. The acquisition duration for the single trials A1, A2, and A3 was 10 s. Two trials for each area were conducted. Hence, a total of 20 s period sampling was obtained for each area at each elevation. This provided sufficient samples to ensure the accuracy of statistics.

The images were analyzed using commercial software (Koncerto II, Seika Digital Image Corp.) based on fast Fourier transform cross-correlation. A multigrid interrogation algorithm was adopted to analyze the images. The interrogation size ranged from $96\times$ 96 to $32\times$ 32 pixels. The final interrogation size was denoted as $M = 32$. A Gaussian distribution function was used to interpolate the subpixels for velocity determination. The output grid resolution was set to 16 pixels (1.6–1.7 mm) by the final 50%-overlapped interrogation window. The velocity data were obtained by calculating the correlations between two images captured at intervals of 5.0×10^{-4} s. Considering that the streamwise velocity within the canopy layer at $z= 0.5H$ was approximately 1.25 m/s, the average movement distance of seeding particles within the canopy layer was estimated to be 5.9–6.3 pixels. This satisfied the technical limitations of PIV data analysis wherein the average movement distance of seeding particles n should be less than $M/2$.

After obtaining the time-series data with a sampling frequency of 2000 Hz, the power spectral densities at various locations in the three measurement areas were determined. We employed a continuous-wave laser. The intervals between images were controlled using a high-speed camera. Therefore, the effective sampling frequency is approximately n/M of the frame rate. In addition, the power spectral density showed that the energy increased in the high-frequency regions, which cannot occur physically owing to noise. Therefore, a low-pass filter of 250 Hz was used to preprocess the data and eliminate high-frequency noise.

3. Statistics

3.1. Spatial distributions of turbulent statistics

To understand the qualitative relationship among the various turbulent statistics within the canopy layer, we determined the spatial distributions of various statistics of the horizontal wind speed v_a defined as $v_a = \sqrt{u^2 + v^2}$.

The temporal average, deviation, and percentile wind speeds $\overline{v_a}$, $v_a^{'}$, and v_{aP} are defined as follows:

$$\overline{v_a} = \frac{1}{T}\int_T v_a(t)dt = \int_{-\infty}^{\infty} p(v_a)v_a dv_a \tag{3.1}$$

$$v_a^{'} = v_a - \overline{v_a} \tag{3.2}$$

$$P = \int_{-\infty}^{v_{aP}} p(v_a)dv_a \tag{3.3}$$

where T is the sampling period of each trial. p and P are the PDF and CDF, respectively, of v_a. The integral time scale τ is defined by the integrated area of the auto correlation function $R(\tau) = \overline{v_a^{'}(t)v_a^{'}(t+\tau)}/\sigma_{v_a}^2$ between 0 and $\tau_{0.1}$ as

$$\tau \cong \int_0^{\tau_{0.1}} R(t)d\tau \tag{3.4}$$

Here, $\tau_{0.1}$ is the time when R crosses 0.1. The PF and GF are defined as follows:

$$GP_{P\%} = \frac{v_{aP}}{\overline{v_a}} \tag{3.5}$$

$$PF_{P\%} = \frac{v_{aP} - \overline{v_a}}{\sigma_{v_a}} \tag{3.6}$$

where σ_{v_a} is the standard deviation of v_a.

Fig. 3 shows the temporally averaged wind speed $\overline{v_a}$, τ, and gust and peak factors $GF_{99.9\%}$ and $PF_{99.9\%}$ defined by the 99.9th percentile $v_{a99.9\%}$ at $z/H= 0.5$ for the three units (A1, A2, and A3). These quantities were defined based on a dataset during $T= 10$ s, and the ensemble average of the two trials was calculated. The integral timescale was normalized using the timescale defined as H/u_{ref}, which represents the mean passing period over a block. In Fig. 3, the white regions indicate the areas where the velocity fields were not determined owing to measurement limitations. Although the distributions of GF and PF were discussed by Hirose et al. [18] at the three heights of $0.1H$, $0.25H$, and $0.5H$ based on the same dataset, we present the reanalyzed data of the GF and PF to explore the relationships among the other statistical values, GP, and PF.

As shown in Fig. 3 (a), the mean wind speed magnitudes and vectors show weak wind speed areas in A1 and A3 owing to the wake flow of the upstream block and the reverse flow in front of the block. In contrast, the flow contraction caused a significant acceleration of the wind in A2. These flow patterns are consistent with those reported in previous numerical simulations (e.g. Refs. [6,32–35]). With regard to the GF distribution, the regions where the GF diminishes corresponds to those where $\overline{v_a}$ speeds up. Although the trend of PF was less evident than that of GF, a similar negative correlation between $\overline{v_a}$ and PF was observed. The tendency of GF and PF to be negatively correlated with the mean wind speed is consistent with previous studies based on CFD [11] and WTE [17,18].

The spatial distributions of τ have not been discussed, particularly that at a height within an urban canopy. Interestingly, Fig. 3 (b) shows that τ has clear spatial distributions affected by the surrounding blocks. In the areas within the wake (A1) and in front of a block (A3), τ is apparently smaller probably because of the weak turbulence. In addition, τ in the strong wind speed regions in A2 is small. This is a plausible trend because a strong advection is likely to cause a rapid reduction in autocorrelation with respect to time. However, the trend is less apparent because the τ in the strong wind region in A1 (e.g., $0.5 < x/H < 1.0$ and $0 < y/H < 0.3$) exhibits the largest values within the canopy. This result implies that τ, which is determined by the auto correlation function, is affected by both advective wind speed and turbulent eddy scale of the flow introduced into the canopy. According to the qualitative observation of the turbulent statistics, the relationship between τ, GF, and PF is ambiguous (the correlation between the peak and the integral time scale is quantified in the latter section) in terms of the spatial distributions.

Further statistics are shown in Fig. 3. The nth-order moment of the velocity component u_i is defined as

$$m_n = \frac{\overline{u_i^{'n}}}{\sigma_{u_i}^n} \tag{3.7}$$

Here, σ_{u_i} is the standard deviation of the velocity component u_i. To determine the nth-order statistics of the velocity components in different directions, the above variables can be substituted with the corresponding components (i.e., v, v', w, and w'). From the definition, the mean and variance of the variables can be derived by the first- and second-order statistics. i.e., $\overline{u^{'1}} = 0$ and $\overline{u^{'2}} = \sigma^2$. For the wind speed, we replace u_i with v_a. By definition, the third- and fourth-order moments are identical to the skewness s_k and kurtosis k_t, respectively. The convergence of the statistics during the measurement period of 20s are explained in Appendix 1. To effectively compare the relationship between the mean

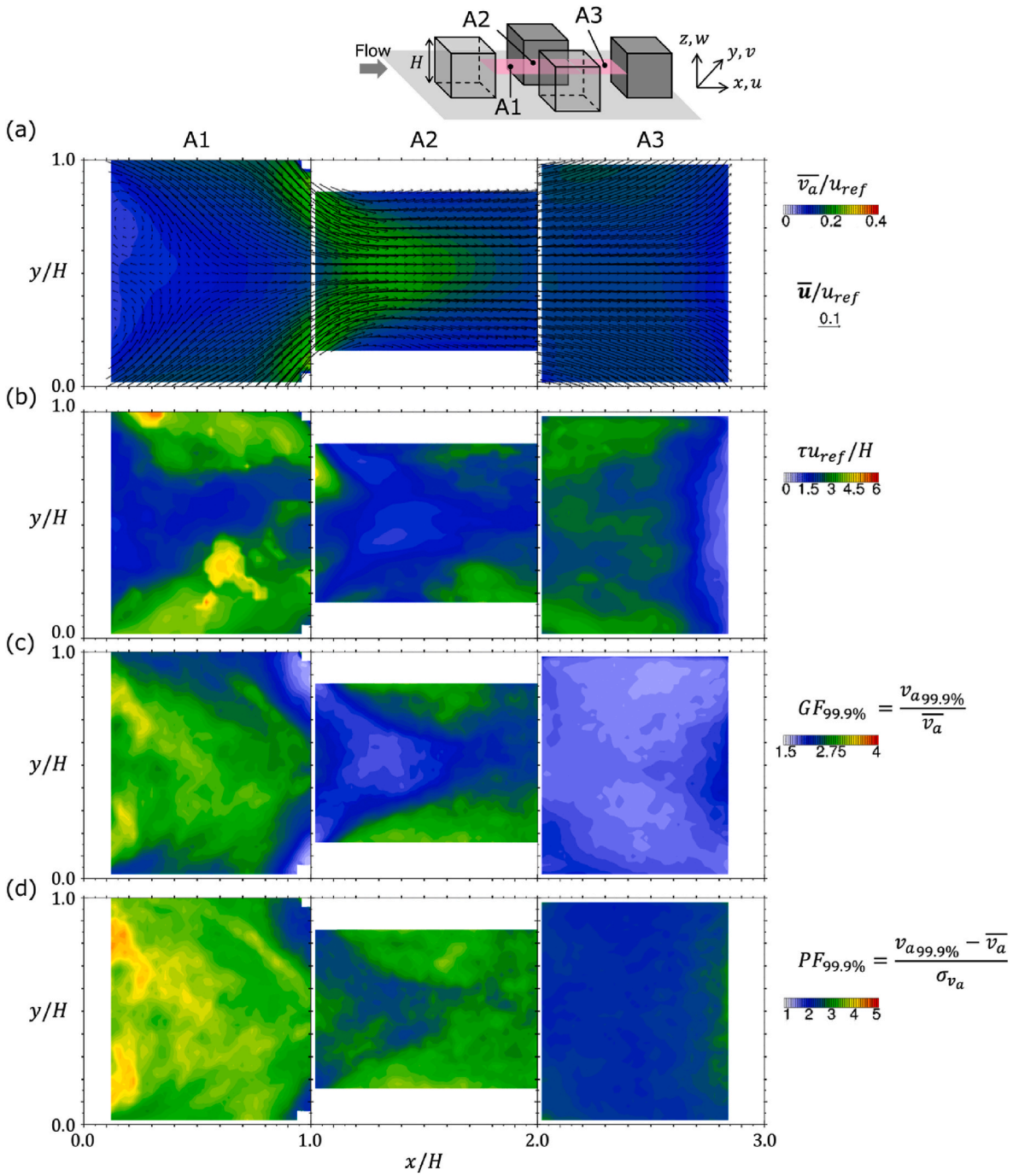

Fig. 3. Spatial distributions of statistical values related to wind speed v_a at $z/H = 0.5$. (a) Mean wind speed $\overline{v_a}$, (b) integral time scale τ. 99.9th percentile wind speed $v_{a99.9\%}$ expressed by the (c) gust factor GF and (d) peak factor PF. u_{ref}: reference wind speed, H: block height, σ_{v_a}: standard deviation of v_a. The white areas indicate areas that were not measured owing to laser reflection and obstruction by the surrounding blocks.

velocity distribution and statistics, the vectors of $\overline{u}$ and $\overline{v}$ are also shown in Fig. 4 (a). In addition, skewness is known as a statistic that shows the PDF asymmetrical extent based on the sign (when s_k is positive, the PDF has a positive long tail, and vice versa). Therefore, a bicolor contour is used only for the skewness graph (Fig. 4 (b)).

As shown in Fig. 4 (a), σ_{v_a} normalized by u_{ref} shows a significant positive correlation with $\overline{v_a}$. In addition, the small integral time scale for A1 and A3 may be attributed to the low turbulence with a low wind speed (Fig. 3 (b)). The value of s_k clearly show that most regions have positive values for A1 and A2, whereas a negative skewness dominates for A3. Because we consider the horizontal wind speed defined by $\sqrt{u^2 + v^2}$, the minimum values of v_a are restricted to zero. Hence, the PDFs in most areas are expected to be positively skewed. However, this result implies that the asymmetric shapes of the PDFs of v_a within a canopy layer vary owing to the complex velocity fields.

In terms of the magnitudes of s_k, k_t, and m_5, the distribution showed patterns similar to those of GF and PF, particularly in A2. That is, small values were observed in the strong wind speed area of A2. Moreover, the GF and PF appeared to be large when these moments became large. This implies that strong wind-speed events are highly influenced by the high-order moments s_k, k_t, and m_5. Although we further discuss the relationship between the moments and strong wind speed in a subsequent

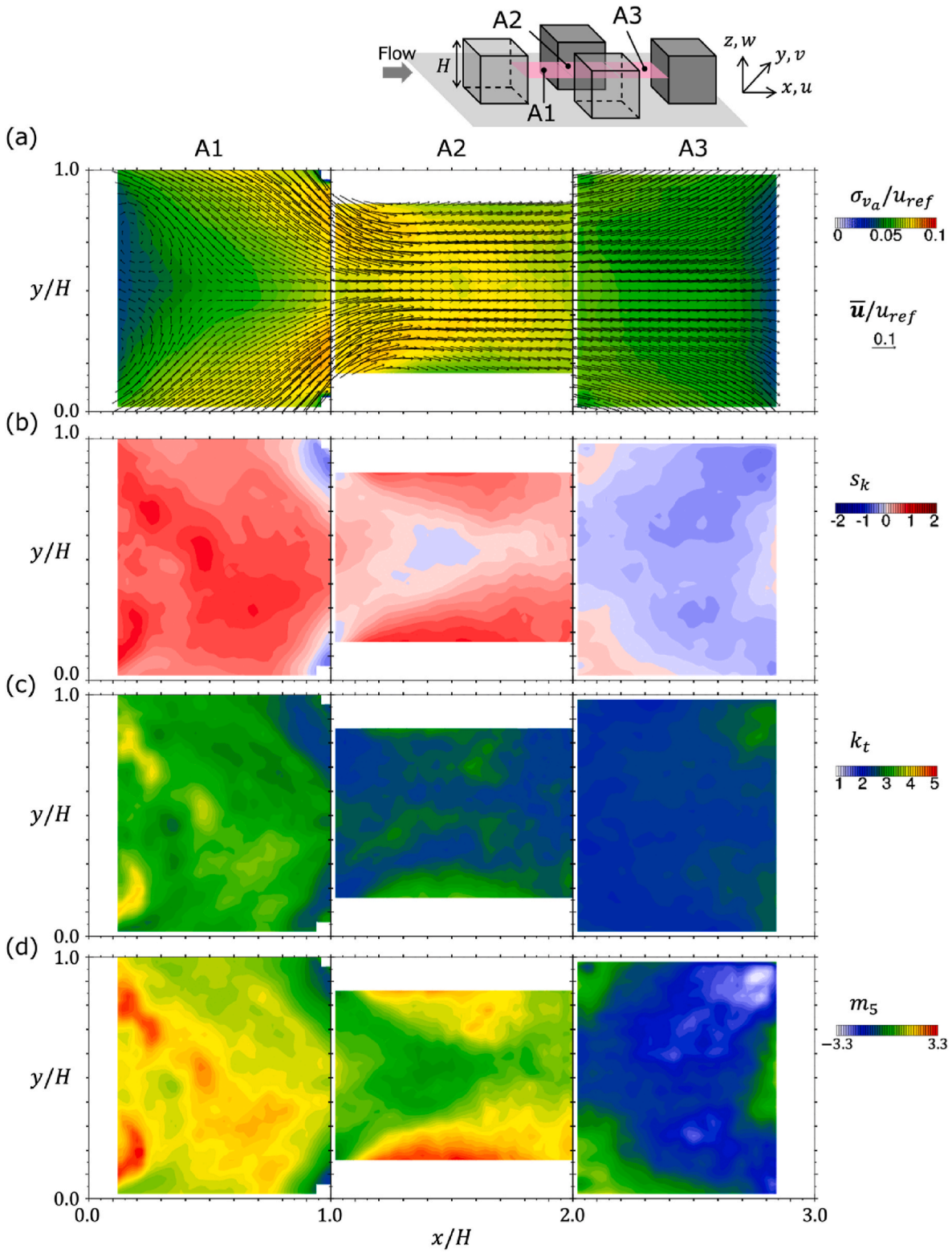

Fig. 4. Spatial distributions of high-order statistics of wind speed v_a at $z/H = 0.5$. (a) Standard deviation σ_{v_a}, (b) skewness s_k, (c) kurtosis k_t, and (d) fifth-order moment m_5.

section, these qualitative discussions indicate the importance of investigating the spatial distributions of high-order moments to clarify why low-occurrence strong wind speed events occur within the canopy.

3.2. PDF and PSD classification by flow patterns

According to recent studies (e.g. Refs. [11,17,21–24,26]), the PDFs at the pedestrian level of a simplified canopy are modeled based on specific distribution functions such as Gaussian or Weibull to express the long-tail shape of the PDFs for wind speeds. The different shapes of the PDFs at each location within a canopy imply that the statistical characteristics of the turbulent flow are altered owing to the presence of blocks in the canopy. In addition, based on previous studies [11,17], the PDFs approach Gaussian distributions when the mean wind speed

increases. These results indicate that there may be mean flow patterns affecting the shapes of the PDFs of the wind speed and velocity components at the pedestrian level. To understand the influential flow patterns within the canopy on the PDFs and turbulent flow, we evaluated the relationship between the PDFs and PSDs based on the flow pattern classification.

Fig. 5 shows the PDFs and PSDs for u, v, and v_a at every five grid points (approximately every $0.05H$) in the x- and y-directions in the three unit areas (A1, A2, and A3) at $z/H = 0.1$. The PSDs at several points within the same canopy were previously reported by Herpin et al. [36]. Before we apply the classifications of the PDFs and PSDs, we confirmed that the PSDs mostly follows the Karman spectrum and are consistent with those in the previous study at $(x/H, y/H, z/H) = (1.5, 0.5, 0.5)$ and $(2.5, 0.5, 0.5)$ (the centers of A2 and A2, respectively). The PDFs and PSDs were classified based on whether the mean streamwise velocity component was positive (positive-flow regions) or negative (reverse--flow regions). The PSDs of turbulent flow are commonly expressed by the von Karman PSD for the streamwise and spanwise velocity components, S_u and S_v as follows [37–39]:

$$\frac{S_u f}{\sigma_u^2} = \frac{4\tilde{f}}{\left(1+71\tilde{f}^2\right)^{5/6}} \tag{3.8}$$

$$\frac{S_v f}{\sigma_v^2} = \frac{2\tilde{f}\left(1+188\tilde{f}^2\right)}{\left(1+71\tilde{f}^2\right)^{11/6}} \tag{3.9}$$

where $\tilde{f} = f\tau$ is the normalized frequency. Hence, two lines are also shown as references defined in the graphs for the PSDs.

The PDFs and PSDs of u are shown in Fig. 5 (a). Although there are numerous sampling points, the PDFs in the positive flow regions ($\overline{u} > 0$) is evidently negatively skewed whereas these are the opposite in the reverse flow regions ($\overline{u} \le 0$). The average s_k in each category is -0.42 and 0.43, respectively. This implies that weak or strong streamwise winds occur infrequently when $\overline{u}$ is positive or negative. Previous studies [40–43] demonstrated that the sweep motion ($u' > 0$ and $w' < 0$) dominates within the urban-like canopy of a staggered layout, whereas the ejection motion ($u' < 0$ and $w' > 0$) becomes significant near the smooth wall or the urban-like canopy in a square layout. Finnigan et al. [42] compared the vertical profiles of the ratio between sweep and ejection for different types of canopies. They demonstrated that most regions

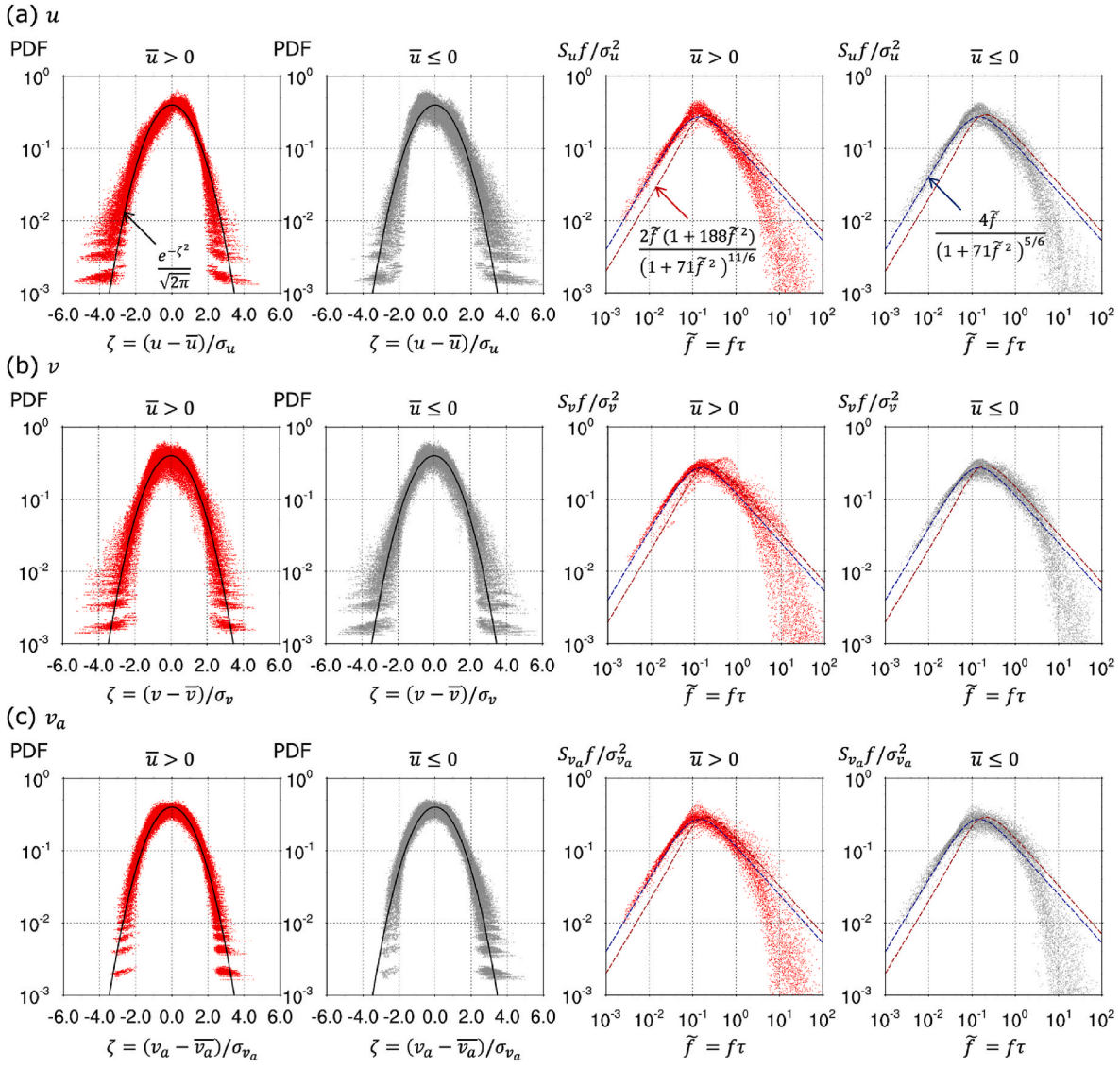

Fig. 5. The relationship between probability density functions, PDFs, and power spectral densities, PSDs, S_{u_i}, by two-class classification of the streamwise ($\overline{u} > 0$) and reverse ($\overline{u} \le 0$) flow regions at $z/H = 0.1$. (a) Streamwise velocity component u, (b) spanwise velocity component v, and (c) wind speed v_a.

within a canopy are dominated by sweep events. In contrast, near the bottom surface of the canopy (approximately $z/H< 0.2$), the ejection is marginally superior to or comparable with sweep events. The percentage of each classification of $\overline{u}> 0$ and $\overline{u} \leq 0$ is approximately 46 % and 54 %, respectively. This indicates that the skewed distributions of the streamwise velocity cancel each other out. This is likely to result in a comparable contribution of the sweep and ejection events at this height. When we characterize the statistical features within a canopy layer, such as sweep and ejection events, the horizontally averaged values are commonly discussed (as observed in the aforementioned previous studies). However, the present analyses demonstrate that the streamwise direction is an important factor in characterizing the PDF shapes.

The differences in the PSDs between the positive and negative flow regions are unclear. Both follow the von Karman spectrum according to Eq. (3.8) with respect to the peaked frequency and slopes in $10^{-3} < \widetilde{f} < 10^{0}$. This is notwithstanding that the measurement height of 0.1H was close to the bottom surface. Good agreement between the PSDs within the canopy and the von Karman spectrum around the peak value has also been reported in previous studies based on field measurements [40].

Fig. 5 (b) and (c) shows the PDFs and PSDs for v and v_a with an identical classification. Unlike u, the differences in PDF and PSD between the positive- and reverse-flow regions are marginal. For the PDFs of v, the distributions are almost symmetrical regardless of the values of $\overline{u}$ because of the geometric symmetry of the flow distribution around the block array. In contrast, the PDFs of v_a are marginally positively skewed compared with the Gaussian distribution. However, the difference in the PDFs based on the classification of $\overline{u}$ is highly marginal. Similarly, the differences in the PSDs for both v and v_a are hardly visible, that mostly follow the von Karman spectrum similar to those of u.

Fig. 6 shows the PDFs and PSDs classified according to whether $|\overline{v}/\overline{u}|> 1$ or not. Because the freestream velocity is expressed as $(u, v) = (u_{ref}, 0)$ above the boundary layer height, this classification indicates that the canopy flow is altered in the spanwise direction owing to the flow separation by front face of the block or wake of the block. The threshold of $|\overline{v}/\overline{u}| > 1$ indicates that the spanwise flow dominates the wind direction, i.e., $Tan^{-1}|\overline{v}/\overline{u}|> 45\ ^{\circ}$. In this classification, the measurement points that satisfy the condition $|\overline{v}/\overline{u}|> 1$ account for approximately 33 %. This indicates that the streamwise velocity component dominated the flow fields even at $z/H = 0.1$.

In Fig. 6 (a), the PDFs of u for both $|\overline{v}/\overline{u}|> 1$ and $|\overline{v}/\overline{u}|\leq 1$ resemble the Gaussian distribution. However, the PDFs for $|\overline{v}/\overline{u}|> 1$ is marginally

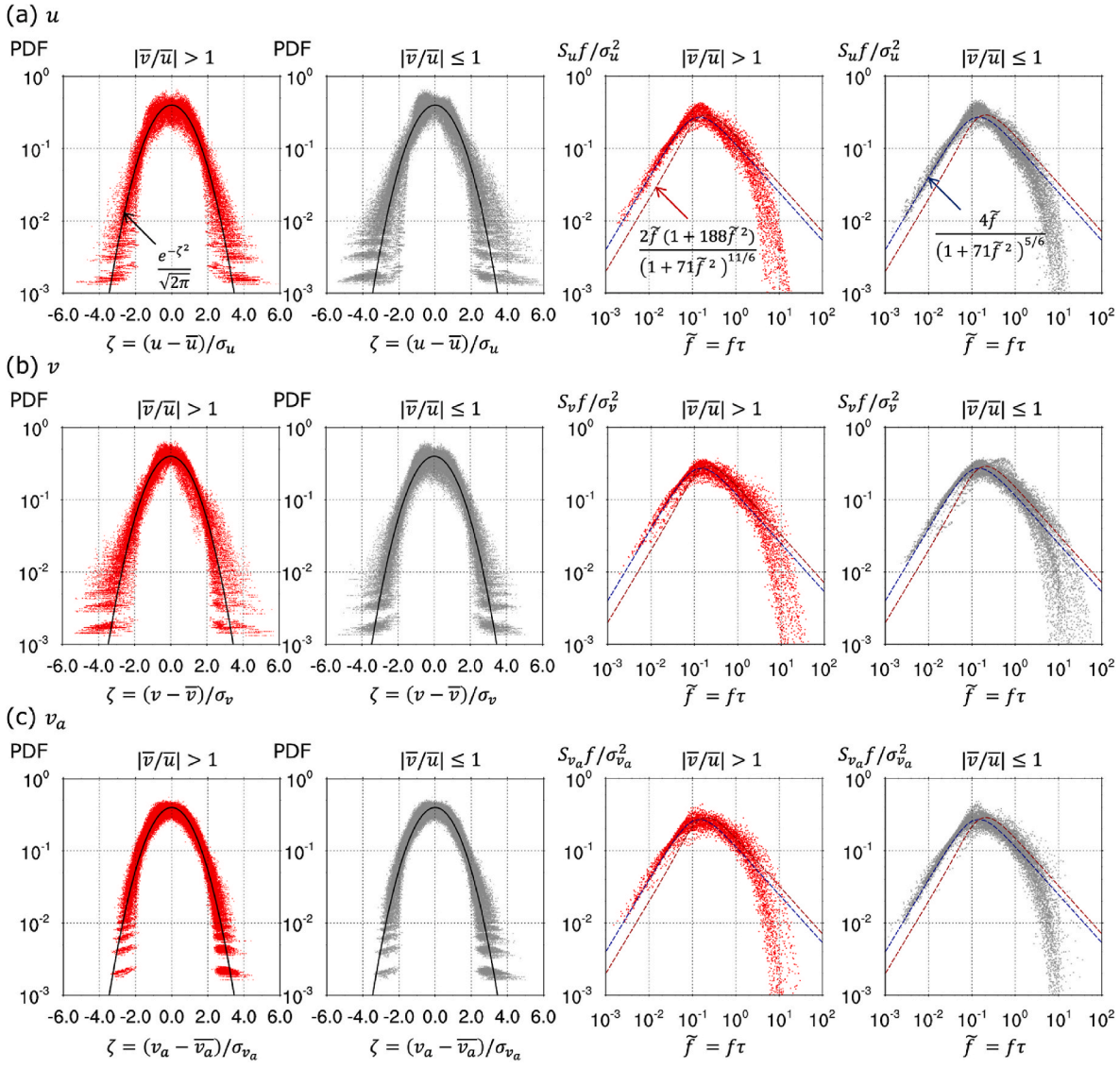

Fig. 6. The relationship between probability density functions, PDFs, and power spectral densities, PSDs, S_{u_i}, by two-class categorization of the spanwise-dominated ($\overline{v}/\overline{u}> 1$) and streamwise-dominated ($\overline{v}/\overline{u} \leq 1$) flow regions for (a) the streamwise velocity component u, (b) spanwise velocity component v, and (c) wind speed v_a.

positively skewed. The skewness is 0.11. In contrast, the shape of the PDFs for $|\overline{v}/\overline{u}| \leq 1$ is sharper than that of the Gaussian distribution. To support this aspect, the kurtosis of this classification is $k_t = 3.4$ (note that the $k_t = 3$ for the Gaussian distribution). In Fig. 6 (b), the PDFs of v for both $|\overline{v}/\overline{u}| > 1$ and $|\overline{v}/\overline{u}| \leq 1$ show similar trends. However, the shape of the PDFs for $|\overline{v}/\overline{u}| > 1$ is sharper than that of the Gaussian distribution, with $k_t = 3.4$. Unlike the differences in PDFs, the PSDs follow the von Karman spectrum. Fig. 6 (c) shows the PDFs and PSDs of v_a. The PDFs agree well with the Gaussian distribution regardless of the $|\overline{v}/\overline{u}|$ values. In addition, the PSDs are well-expressed in the von Karman spectrum.

According to these results, for the velocity components, the PDFs appear to become sharper when the wind within the canopy is unidirectional. However, a similar alteration of PDFs owing to canopy flow is marginal. In addition, the variation in the PSDs is imperceptible. This is probably because the large-scale turbulence with the integral time scale, namely, the peaked value of the PSDs, dominates the entire turbulence kinetic energy and overall PSD shapes. Consequently, the PSDs followed the von Karman spectrum. In addition, the present datasets were low-passed-filtered by 250 Hz to remove the experimental noise.

With regard to the marginal variation in PSDs, further investigation is required to clarify whether the canopy elements significantly affect the PSDs because we employed filtering at 250 Hz to remove the measurement noise in the experiments (the effect can be observed in the rapid reduction of the PSDs when $\widetilde{f} > 10^0$). In previous studies, the effects of canopy elements on PSDs were explained theoretically or experimentally. For example, Finnigan et al. [44] explained that the wake energy production by canopy elements generates canopy-scale turbulence. This, in turn, alters the slope of the PSDs in the high-frequency range. We could not identify a similar alternation in the PSDs probably because of the sampling frequencies in the PIV. Herpin et al. [36] also reported the PSDs within the same cubical canopy using laser doppler anemometry; however, their measurements were also in a low frequency and unclear increase of the PSDs in high-frequency ranges. Meanwhile, Michioka et al. [45] experimentally speculated that the canopy elements in a square layout generate a low-frequency turbulence in a transient situation with a limited number of canopy elements. Both the studies indicated that canopy elements may alter the PSDs from the typical von Karman spectrum, which is not visible in our datasets. Because we employed a fetch longer than that applied by Michioka et al. [45] with different block layouts, the turbulence generation in the low-frequency mode may not have been apparent. Because of these marginal variations in the PSDs, we could not identify either a clear relationship between the shapes of the PDFs and PSDs or an apparanet alternation of PDFs. Because the standard deviation is expressed as $\sigma_u^2 = \int_{-\infty}^{\infty} u'^2 p(u')du' = \int_{-\infty}^{\infty} S_u(f)df$using a PDF and PSD, we need to further investigation to clarify the relationship between them in the future study.

4. Relationship between statistics and strong wind

4.1. Statistical correlation among statistics, GF and PF

To quantify the statistics that dominantly affect the GF and PF, we investigated the relationship between the high-order statistics of, k_t, m_5

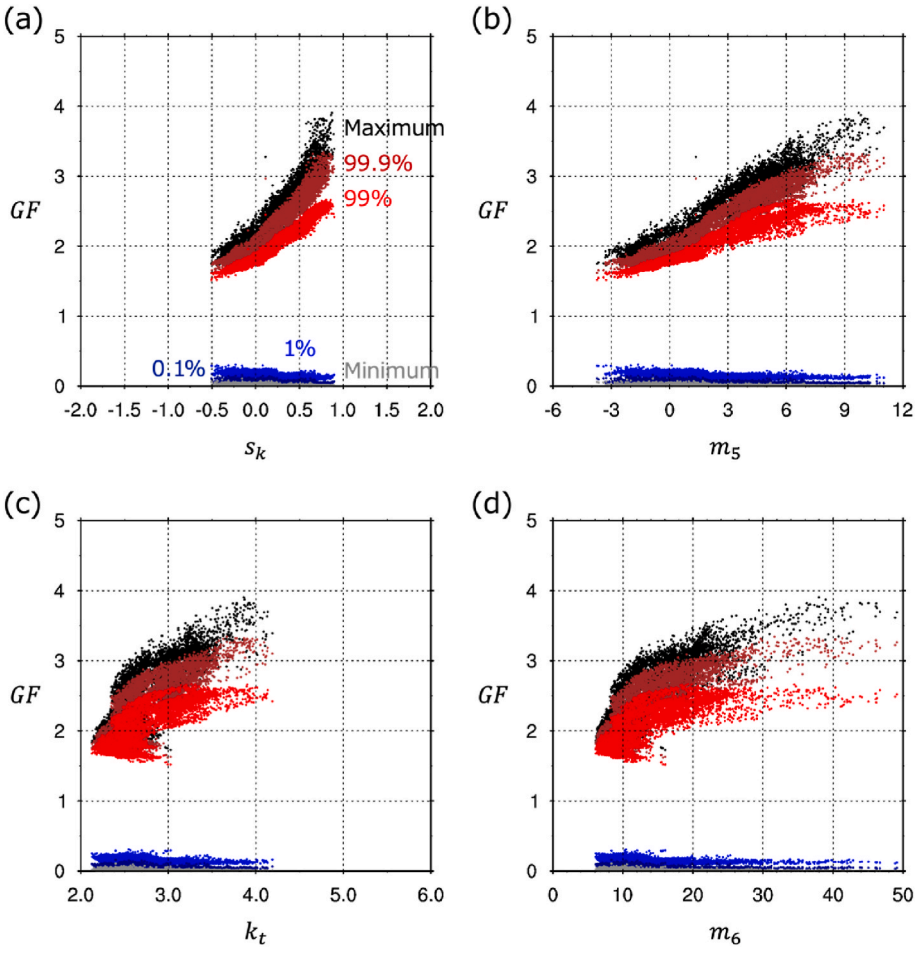

Fig. 7. Relationship between the GF and moments of the wind speed v_a at $z/H = 0.5$. (a) Skewness, (b) fifth-order moment, (c) kurtosis, and (d) sixth-order moment. The maximum (99.9th and 99th) percentiles represent strong wind speeds, whereas the minimum (0.1st and 1st) percentiles indicate the weak-wind-speed events.

and m_6, with GP or PF. To define GF and PF, we selected the maximum (99.9th and 99.0th) percentile values for strong wind speeds and minimum (0.1st and 1.0th) percentile values for weak wind speeds.

Fig. 7 shows the correlation between the higher-order moment (horizontal axis) and GF (vertical axis) at z/H= 0.5 in three unit areas (A1, A2, and A3). Regardless of the order of the moments, the GF of weak wind speeds had a negligible correlation with the moments. In contrast, the GF of strong wind speeds were positively correlated with the moments. In addition, the correlation between the GF and odd-order moments (i.e., s_k and m_5) appeared to be more apparent than that between the GF and even-order moments. Moreover, the relationships between the GF and moments were attenuated when the order of moments increased. Although we expected that s_k to m_6 may vary by 10 % (Please refer to Appendix 1), the clear difference in the tendency between the GF and even- or odd-order moments can be hold with such expected variations.

Fig. 8 shows the relationships between the PF and moments at z/H= 0.5 in the three unit areas (A1, A2, and A3). In the case of the PF, the trend shown in the relationship between the GF and moments was apparent for strong wind speeds. That is, the odd-order moments (namely, s_k, and m_5) were positively and linearly correlated with the PF, and the s_k displayed steeper slopes in the relationship between the PF and moments than m_5. In addition, the PF of weak wind speeds showed a positive correlation with the odd-order moments. In contrast, the correlation between the PF and even-order moments was obscure, particularly for m_6.

The positive correlation of the PF of the strong wind speeds with the odd-order moments indicates that rare and extreme winds cause the PDFs to have a long-tail shape on the positive side because positive odd-order moments imply that the PDFs are positively skewed. Simultaneously, it shortens the other edges of the PDFs. As a result, the PF of strong wind speeds increased, whereas that of weak wind speeds decreased when the odd-order moments were large. In contrast, the positive or negative correlations between the even-order moments and PF of the strong or weak wind speeds imply that an increase in the sharpness of the PDF shapes reduced the frequencies of the extreme values but expanded the PDFs to a wider range. This caused an increase in the magnitude of the extreme values.

To quantify the relationships between the GF, PF, and statistical properties of the velocity fields at three heights of the three units (0.1H, 0.25H, and 0.5H of A1, A2, and A3), Figs. 9 and 10 show the correlation coefficients between the GF or PF (values of y axis in Figs. 7 and 8) and the statistics (the values of x axis in Figs. 7 and 8). In addition to the high-order moments shown in Figs. 7 and 8, $\overline{v_a}$, σ_{v_a}, and τ are included in the figure. The correlation coefficient C of the datasets of x_i and y_i (i= 1 to N, where N is the data number.) is defined as $C = \Sigma_i x_i y_i / (\Sigma_i x_i^2 \Sigma_i y_i^2)^{0.5}$).

Fig. 9 (a) shows the correlations between the GF of weak or strong wind speeds and the statistics. Overall, the correlation between the GF of weak wind speeds and moments was smaller than that between the GF of strong wind speeds and moments. This indicates that the magnitude of wind speeds in the lower tail range of the PDFs may be determined irrespective of these statistical values. Because the magnitude of v_a is limited to zero by the definition $v_a = \sqrt{u^2 + v^2}$, the lower values of v_a

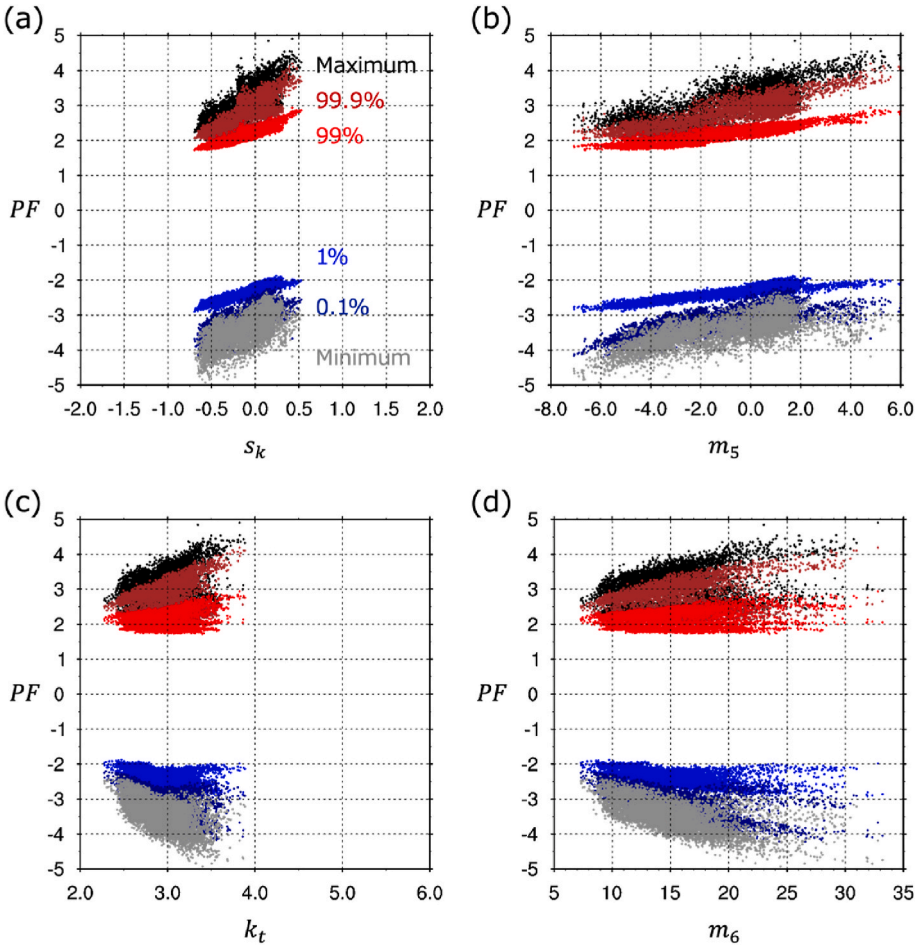

Fig. 8. Relationship between the peak factor and higher-order statistics of the streamwise velocity component u at z/H = 0.5. (a) Skewness, (b) fifth-order moment, (c) kurtosis, and (d) sixth-order moment. The maximum (99.9th and 99th) percentiles represent strong wind speed events, whereas the minimum (0.1st and 1st) percentiles indicate the weak-wind-speed events.

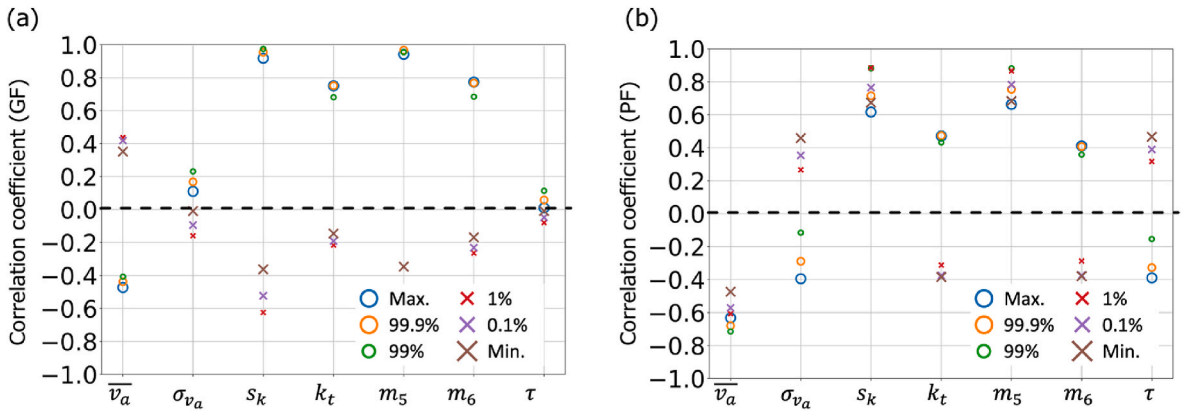

Fig. 9. Correlation coefficient between statistics of v_a and (a) the gust factor *GF* or (b) peak factor *PF* in three units (A1, A2, and A3) at three heights ($0.1H$, $0.25H$, and $0.5H$). The maximum (99.9th and 99th) percentiles represent the strong wind speed events, whereas the minimum (0.1st and 1st) percentiles indicate the weak wind speed events. The selected statistics are the mean $\overline{u_i}$, standard deviation σ_{u_i}, skewness s_k, kurtosis k_t, higher-order moments, m_5, m_6, and τ.

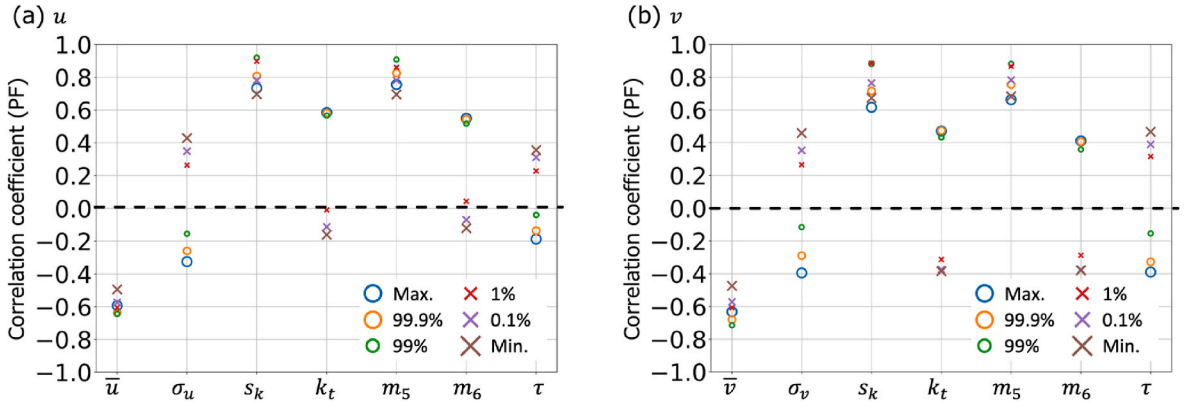

Fig. 10. Correlation coefficient between the peak factor *PF* and statistics for (a) the streamwise and (b) spanwise velocity components in three units (A1, A2, and A3) at three heights ($0.1H$, $0.25H$, and $0.5H$). The maximum (99.9th and 99th) percentiles represent the strong wind speed events, whereas the minimum (0.1st and 1st) percentiles indicate the weak wind speed events. The selected statistics are the mean $\overline{u_i}$, standard deviation σ_{u_i}, skewness s_k, kurtosis k_t, higher-order moments, m_5, m_6, and τ.

may be determined to be nearly zero irrespective of the magnitude of the moments. In contrast, the correlation between the GF of strong wind speeds and moments was significantly stronger. In addition, the correlations decreased gradually with an increase in the order of moments. This is plausible because the lower-order moments are more influential on the shape of the PDFs based on a previous study employing the orthogonal decomposition of the PDFs by Gram–Charlier series expansion (e.g. Ref. [23]). This results in a large influence of the lower-order moments on the GF for strong wind speeds.

Another noteworthy aspect is that $\overline{v_a}$ and σ_{v_a} have relatively loose correlations with the GF. The GF is defined using the mean (Eq. (3.5)). This implies that the GF is assumed to be independent from $\overline{v_a}$. This assumption is mostly reasonable. However, the weak correlation between the GF and $\overline{v_a}$ indicates that the spatial variation in GF is partially owing to the spatial variation in $\overline{v_a}$ as well. Moreover, the correlation between the GF and τ is highly marginal. From our qualitative discussion of the spatial distribution of the GF and τ (Fig. 2), we anticipated that the GF and τ may be correlated because τ is a time scale to represent the peak of the PSDs. This is demonstrated by the good agreement between the PSDs and von Karman spectrum (the normalized frequency of $\widetilde{f} = f\tau$ is employed in the graphs). However, the statistical analyses addressing the entire canopy area at the three heights showed that the correlation is significantly small. This indicates the existence of locations where τ do not affect GF.

Fig. 9 (b) shows the correlation between the PF and statistics. Although the PF with weak wind speeds showed a tighter correlation than the GF, the other trends were highly similar to those of the GF. That is, the correlations decreased gradually with the order of the moments. $\overline{v_a}$ and σ_{v_a} showed relatively small correlations, and τ was negligibly correlated with the PF. Because the PF is defined using $\overline{v_a}$ and σ_{v_a} (Eq. (3.6)), the correlation of the PF with $\overline{v_a}$ and σ_{v_a} is assumed to be insignificant. Although the small correlation indicates that the PF is almost independent of σ_{v_a}, the marginal correlation with $\overline{v_a}$ of -0.4 is consistent with the spatial variation in PF corresponding to $\overline{v_a}$ (Fig. 3 (a, d)). The significant positive relationship of the PF with the moments (s_k, k_t, m_5, and m_6) over 0.8 also indicates that considering s_k and k_t is essential to model the PF according to the considerable spatial distributions (Fig. 4 (c, d)). In addition, taking into account m_5–m_6 is ideally desirable for the modeling the PF if the s_k and k_t distributions are not sufficient to predict low-occurrence wind speeds. In contrast, higher-order moments are not necessary for predicting the PF.

As shown by the relationship between the GF and τ, the correlation between the PF and τ is marginal. In Fig. 3, the spatial distribution of the PF and τ in the high speed regions in A2 could be observed. However, regions where a clear correlation between the PF and τ cannot be verified also exists. Eventually, the correlation between the PF and τ within the entire horizontal unit of the canopy at the three heights revealed that the correlation is significantly small.

Fig. 10 shows the correlation coefficients between the PF and the statistics of u and v. It is noteworthy that the odd-order moments have a

stronger correlation with the PF than the even-order movements. In addition, the PF of the strong wind speeds clearly displays larger values than those of the weak wind speeds for both u and v. Moreover, the correlations between the PF and the mean, standard deviation, and integral time scale are relatively small. These results imply that the peak velocity components are affected by s_k,m_5, and m_7 rather than by k_t, m_6.

These results clearly show that both GF and PF are influenced by the moments of the wind speed or velocity components. In a previous study, Zainol et al. [27] determined the correlation coefficient between the velocity component deviation from the mean and moments of an approaching flow in a wind tunnel generated by spires and roughness. They demonstrated a significantly strong correlation between the moments and deviations. These results indicate that the peak wind speeds and velocity components can be determined using these statistical values. If we can determine the GF or PF using statistics, it is advantageous because statistical quantities, such as moments, are more convenient to obtain than directly calculating the peak values. In addition, recent studies by Wang et al. [23,26] and Seta et al. [24] employed the GCS from the second-to sixth-order models (i.e. the second-to sixth--order moments were implemented to predict the PDFs; please refer to the GCS model in Ref. [23]). They demonstrated that the third- and fourth-order models accurately predicted the percentiles of the wind speed and velocity components. This is also plausible because the present statistical analysis showed that s_k and k_t affect the GF and PF.

A concern regarding the present observations is that the correlation between the PF and τ was invisible. Although we quantitatively acknowledge the consistency in the spatial distribution of the PF and τ in Fig. 3, the overall correlation at the three unit areas and three heights was significantly small. The correlation between the peak value and τ has been reported earlier. For example, Efthimiou et al. [20] demonstrated that the PF of the maximum velocity is proportional to $(\tau/T)^{1/3}$, where T is the total sampling time. This indicated that the PF is positively correlated with τ. Although we employed percentiles to define the PF to address both strong and weak wind speeds as well as the maximum values, the correlations of the maximum and minimum wind speeds with the PF are rather marginal. We also verified from the scatter distribution that the PF is almost a plateau with respect to τ. A likely factor causing this discrepancy is the relatively small variation in τ within the canopy. Therefore, the correlation the PF is unclear. However, with regard to the impact of τ on the strong and weak wind speeds, we need to investigate further based on different types of turbulent flow at pedestrian levels.

4.2. Theoretical relationship among PF, s_k, and k_t

According to the previous analyses in Section 3.2, the relationship between the PDFs and PSDs is ambiguous in the present dataset. Meanwhile, the high-order statistics, particularly s_k and k_t, display significant positive correlations with the PF in Section 4.1. This implies that the PF can be predicted by incorporating these statistics. In addition, recent studies predicted peak wind speeds using stochastic methods based on theoretical distribution functions by employing high-order statistics [21–24,26]. Therefore, in this section, we investigate the relationship between these theoretical predictions and experimental data in terms of the PF.

The Weibull distribution is commonly adopted to fit wind speeds and analyzing the PDF in practical applications to sufficiently understand the wind field. Wang and Okaze [21,22] employed a two-parameter Weibull distribution to describe the instantaneous wind speed:

$$p(x)=\left(\frac{\beta}{\alpha}\right)\left(\frac{x}{\alpha}\right)^{\beta-1}\exp\left(-\left(\frac{x}{\alpha}\right)^{\beta}\right) \tag{4.1}$$

Here, x is the random variable. $\alpha>0$ and $\beta>0$ are the scale parameter and shape parameter, respectively. Wang and Okaze [21,22] applied the Weibull distribution for wind speed (i.e., $x=\sqrt{u^2+v^2+w^2}$). However, we applied the function for the velocity components u, v and the horizontal wind speed v_a. If the wind speed and velocity components follow the distribution function, the PF (defined by the percentile value) is determined by

$$PF=\frac{x_P-\bar{x}}{\sigma_x}=\frac{[-\ln(P)]^{1/\beta}}{[\Gamma(1+2/\beta)-\Gamma^2(1+1/\beta)]^{1/2}} \tag{4.2}$$

where x_P is the percentile value; $\bar{x}$ and σ_x are the mean and standard deviation, respectively; P is the cumulative density in percentage; and $\Gamma(\xi)=\int_0^\infty x^{\xi-1}e^{-x}dx$ represents the Gamma function. In Eq. (4.2), the PF of a random variable following the Weibull distribution is determined only by the Weibull parameter β and exceedance probability P.

In addition, as Wang and Okaze [21,22] explained, s_k is expressed by an implicit function of the Weibull parameter β as [46]

$$s_k=\frac{\Gamma\left(1+\frac{3}{\beta}\right)-3\Gamma\left(1+\frac{2}{\beta}\right)\Gamma\left(1+\frac{1}{\beta}\right)+2\Gamma\left(1+\frac{1}{\beta}\right)^3}{\left(\Gamma\left(1+\frac{2}{\beta}\right)-\Gamma\left(1+\frac{1}{\beta}\right)^2\right)^{3/2}} \tag{4.3}$$

These relationships indicate that the PF can be expressed as a function of s_k. Similarly, the kurtosis k_t is expressed by an implicit function of the Weibull parameter β as [46]

$$k_t=\frac{\left(\Gamma\left(1+\frac{4}{\beta}\right)-4\Gamma\left(1+\frac{3}{\beta}\right)\Gamma\left(1+\frac{1}{\beta}\right)+6\Gamma\left(1+\frac{2}{\beta}\right)\Gamma\left(1+\frac{1}{\beta}\right)^2-3\Gamma\left(1+\frac{1}{\beta}\right)^4\right)}{\left(\Gamma\left(1+\frac{2}{\beta}\right)-\Gamma\left(1+\frac{1}{\beta}\right)^2\right)^2} \tag{4.4}$$

indicating that the PF is also expressed as a function of k_t.

These relationships are also interpreted as $k_t\equiv k_t(\beta(s_k))=k_t(s_k)$. That is, the distribution function determines the relationship between s_k and k_t for the Weibull distribution.

Another approach was proposed by Seta et al. [24] and Wang et al. [23,26] based on a modified Gaussian distribution using the GCS expansion. The GCS is a series expansion of the Gaussian distribution function with the higher-order statistics that directly uses higher-order moments as parameters to describe the PDFs [25]. Thus, low-occurrence wind speeds can be predicted from higher-order statistics using the GCS method. This method was validated by Wang et al. [23,26] and applied successfully to describe the approaching flow by Zainol et al. [27]. Using the fourth-order GCS model, the distribution function can be expressed as

$$p(\zeta)=\left(1+\frac{s_k}{6}\zeta\left(\zeta^2-3\right)+\frac{k_t-3}{24}\left(\zeta^4-6\zeta^2+3\right)\right)\frac{e^{-0.5\zeta^2}}{\sqrt{2\pi}} \tag{4.5}$$

Here, $\zeta=(x-\bar{x})/\sigma_x$ is the standardized random variable of x. When $s_k=0$ and $k_t=3$, $p(\zeta)$ is identical to a Gaussian distribution. Because the percentile value is defined by Eq. (3.6), the PF is expressed as a function of s_k and k_t (i.e., $PF\equiv PF(s_k,k_t)$) when a random variable follows the PDFs based on the GCS.

Besides, the relationship in the Weibull distribution using $k_t\equiv k_t(s_k)$ can be incorporated into the GCS model. That is, the GCS + Weibull distribution yields the following PDFs:

$$p(\zeta)=\left(1+\frac{s_k}{6}\zeta\left(\zeta^2-3\right)+\frac{k_t(s_k)-3}{24}\left(\zeta^4-6\zeta^2+3\right)\right)\frac{e^{-0.5\zeta^2}}{\sqrt{2\pi}} \tag{4.6}$$

This indicates that $PF\equiv PF(s_k)$. The relationship $k_t\equiv k_t(s_k)$ can be solved numerically based on the inverse function of $s_k(\beta)$ using a numerical calculation, e.g., the Newton–Raphson method. Hence, we can determine $k_t\equiv k_t(\beta)$.

In the following section, we compare the PF determined from the experimental data with those of the Gaussian, Weibull, GCS, and GCS + Weibull distributions.

4.3. Relationship among PF, s_k, and k_t

To verify the validity of $k_t \equiv k_t(s_k)$ in the Weibull distribution for applying the combination model of the Gaussian and Weibull distributions, Fig. 11 shows the relationship between s_k and k_t of u, v, and v_a at the three measurement heights $0.1H$, $0.25H$, and $0.5H$. The dashed line indicates the relationship determined by the Weibull distribution by solving the implicit functions with respect to β in Eqs. (4.3) and (4).4): For the components u and v, the relationship between s_k and k_t basically follows the theoretical line using a Weibull distribution. Although the variations appear larger when $s_k \sim 0$ and $k_t = 3$, these gradually approach the theoretical line when s_k increases. In addition, the agreement with the line for v_a is more prominent. Although the deviation from the line indicates that the random variable does not stringently follow the Weibull distribution, the overall tendency between s_k and k_t shows that k_t can be approximated by s_k by assuming a general tendency of the Weibull distribution.

Fig. 12 shows a comparison of the PF with s_k and k_t for the velocity components u and v. The four lines for each percentile value indicate the PF derived theoretically from the Gaussian, Weibull, GCS, and GCS + Weibull distributions. The line for the GCS assumes that $k_t = 3$ to reduce it to a third-order model (Eq. (4.5)). Before investigating the relationship between the experimental data and these lines, it is worthwhile to discuss the differences among the four theoretical lines. Because the Gaussian distribution is not a function of s_k or k_t, it provides constant values of PF depending on the exceedance percentage P. When $s_k < 0.5$, the difference in the four theoretical lines is marginal for the 99.9th and 99th percentile values. These display an increasing tendency with the PF. In contrast, the PF obtained by the Weibull distribution is larger than those obtained by GCS and GCS + Weibull in the range of $s_k > 0.5$. With regard to the PF by the weak wind speeds of the 1st and 0.1st percentile values, the discrepancies between the theoretical lines are marginal when $-0.5 < s_k < 0.5$. However, these increase gradually when the magnitude of s_k increases. The larger difference among the theoretical lines for the large values of skewness indicates that a marginal difference in the employed model may cause a significant difference in the low-occurrence frequency and magnitude when a distribution function is skewed significantly. With regard to Fig. 12 (b, d), the theoretical lines of the Gaussian, Weibull, and GCS distributions are shown for the percentile values of 0.1, 1, 99, and 99.9 % exceedance probabilities. Because the GCS + Weibull model is a third-order model assuming that $k_t \equiv k_t(s_k)$, it has been excluded from Fig. 12 (b, d). The theoretical lines of the GCS display a monotonic increase with kt for the 99th and 99.9th percentiles, whereas those of the 0.1st and 1st percentiles decreases with k_t. In contrast, those using the Weibull distribution show a peaked k_t with respect to the PF. This indicates that the PF is a multivalue function of k_t.

In Fig. 12 (a) and (c), the experimental data show a significantly good agreement with the lines of the Weibull and GCS + Weibull distributions for the 99th and 99.9th percentiles. The value obtained using the GCS agree well with the experimental data. However, the deviation in the large s_k is significant. The improvement in the GCS using the Weibull distribution indicates that k_t also increases with increasing s_k (as shown in Fig. 10) for the distributions of the velocity components. In contrast, the GCS with $k_t = 3$, which is a third-order model, cannot effectively represent a similar relationship. However, the GCS is advantageous because the model can change using the different values of k_t. This may improve PF prediction. The weak wind speeds of the 0.1st and 1.0th percentile values also show good agreement with the GCS + Weibull distribution. The prediction using only the Weibull distribution marginally overestimated the values compared with the those by GCS + Weibull distribution. It is worth mentioning that the prediction by these theoretical models is applicable regardless of the velocity component, as shown in Fig. 12 (a) and (c). However, it should be noted that the general tendency can be predicted using these models. Meanwhile, the deviation from the line to the experimental data is of the order of 1.0 for PF, particularly for 99.9 % with a large skewness and 0.1 % with a small skewness. Hence, for a precise prediction, we need to consider a more sophisticated model than Weibull or GCS. Nonetheless, these analyses clearly demonstrated that skewness is an influential parameter for PF. Wang and Okaze [21,22] also demonstrated that the PF can be predicted by s_k using a Weibull distribution based on the wind speed determined by CFD at the pedestrian level around an isolated block array in a square layout. The data presented in Fig. 11 were determined based on the experiments. These are also consistent with their analyses based on CFD in terms of low-occurrence strong wind speeds.

Fig. 12 (b) and (d) shows the relationship between PF and k_t. It is noteworthy that the experimental data show a multivalue distribution with respect to k_t. The peak value of k_t with respect to PF is approximately $k_t = 1.9$. Similar multivalue characteristics were predicted effectively by the Weibull distribution although the lines deviated from the experimental data. The predictions of the 99.9th and 99th percentiles by the Weibull distribution showed relatively good agreement with the experimental data, particularly when $k_t >$ three. In contrast, the lines predicted by the Weibull distribution showed smaller values for the magnitude of the PF for the 0.1st and 1st percentiles. The prediction by the GCS cannot show multivalue functions. It increases or decreases monotonically for a strong or weak velocity with increasing kurtosis. With regard to the prediction of weak velocity, the monotonic decrease in the PF by the GCS was more favorable than that by the Weibull distribution. Similar tendencies were also observed for the velocity component v.

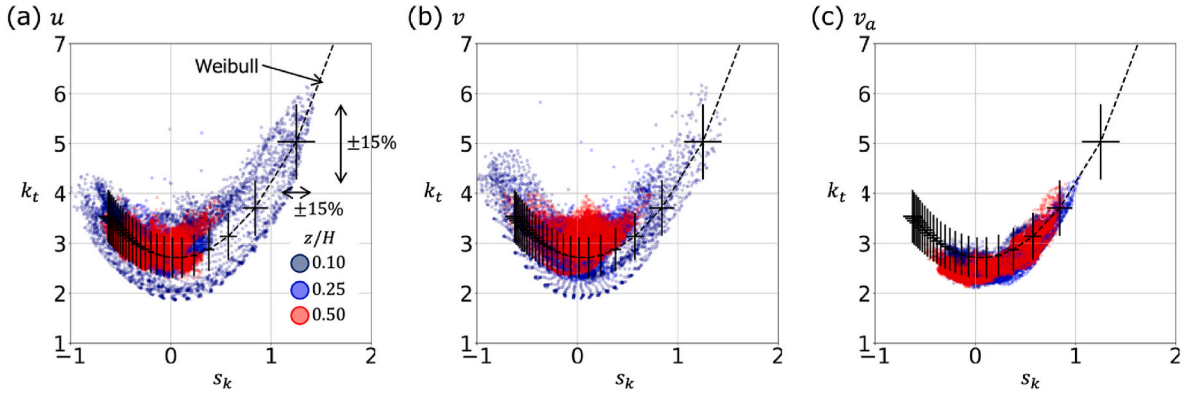

Fig. 11. Relationship between skewness s_k and kurtosis k_t of (a) the streamwise velocity component u, (b) spanwise velocity component v, and (c) wind speed v_a. The dashed line indicates the relationship $k_t \equiv k_t(s_k)$ of a random variable following the Weibull distribution. The error bars indicate ±15% expected variations of the statistics (Please refer to Appendix 1).

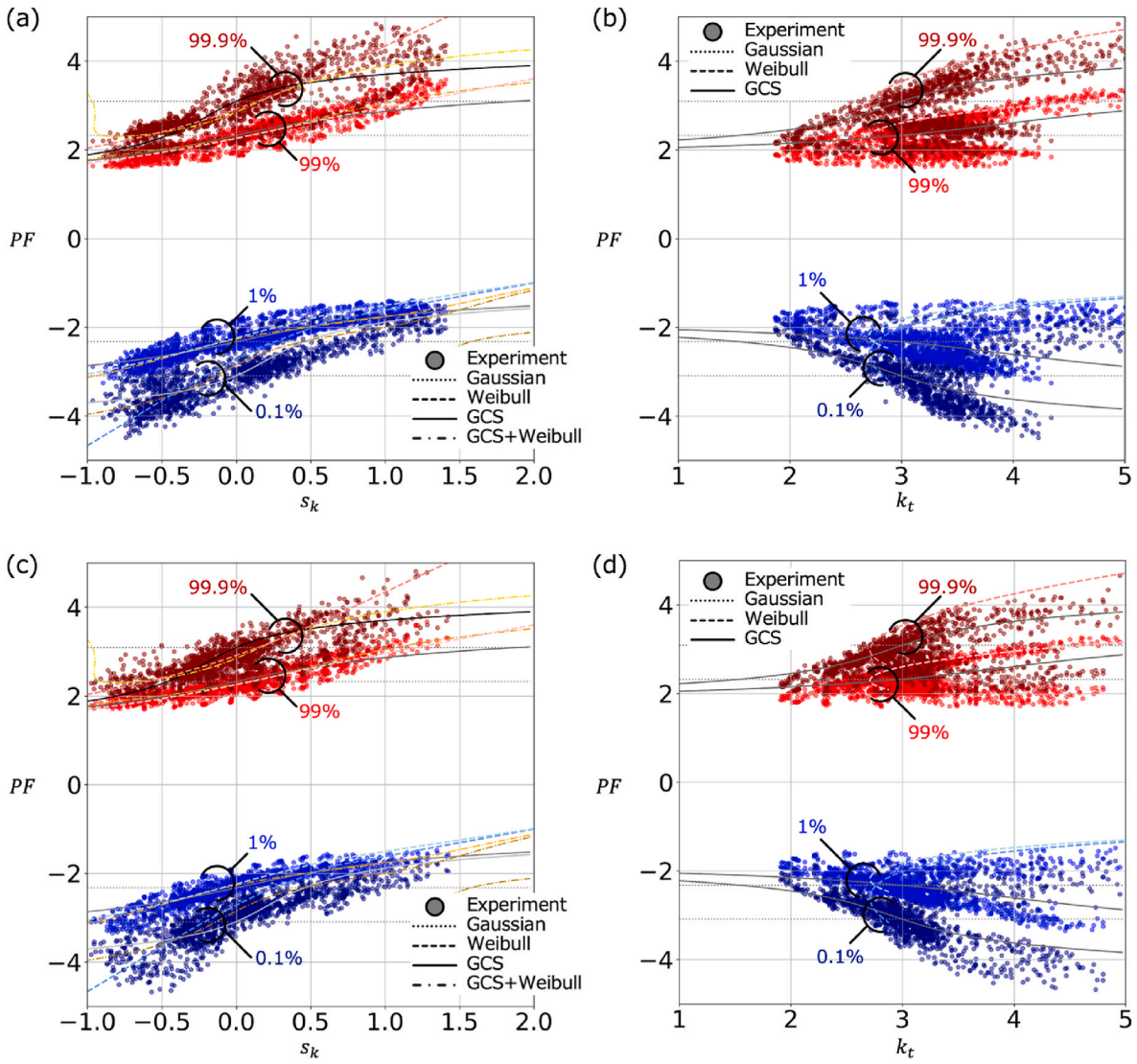

Fig. 12. Relationship between the peak factor *PF*, and (a,c) skewness s_k and (b,d) kurtosis k_t for (a,b) the streamwise velocity component u and (c,d) spanwise velocity component v at $z/H = 0.1$. The lines represent the relationship determined by the Gaussian, Weibull, and Gram–Charlier series (GCS) distributions. GCS + Weibull indicates the relationship obtained by GCS when k_t is modeled by s_k based on the Weibull distribution in Fig. 10. The selected infrequent wind events are the maximum (99.9th, 99th, 1st, and 0.1st percentiles) and minimum.

Fig. 13 compares the theoretical predictions and experimental data as a function of s_k or k_t for the horizontal wind speed v_a at the three heights $0.1H$, $0.25H$, and $0.5H$. The relationship between PF and s_k are shown. The experimental data agree significantly with the predictions by Weibull and GCS + Weibull for the 99th, 99.9th, and 1st percentiles regardless of the measurement heights. Only for the PF defined by 0.1 %, both Weibull and GCS + Weibull distributions overestimate the magnitude of the weak wind speed. Fig. 13 (d)–(f) compares the prediction among the Weibull, GCS + Weibull models, and the experiment as a function of k_t. Similarly, the predictions of the 99th, 99.9th, and 1st percentiles are reasonable. The good agreement with the predicted values is attributed to the small variation in the PF of the velocity components, as shown in Fig. 11.

Owing to the limitation of the k_t of a random variable following the Weibull distribution, the theoretical line by the Weibull distribution cannot adopt a k_t less than 2.8. Meanwhile, the GCS model can expand the lines below the threshold. Because the experimental data also adopts values of k_t between two and three, the prediction by GCS is advantageous in terms of the wider coverage of k_t.

5. Conclusions

We analyzed the velocity datasets within an urban canopy consisting of cubes with H= 0.1 m arranged in a staggered layout with a packing density of 25 %. The measurements were performed at the three heights $0.1H$, $0.25H$, and $0.5H$ by PIV [18]. The purpose of this study was to understand the relationship between low-occurrence velocities and other turbulent statistics to validate previously reported statistical methods [21–24,26] in which extreme wind speeds were predicted using high-order statistics. Accordingly, we investigated how the urban canopy elements affect the probability density function (PDF) and power spectral density (PSD) to understand the physical interpretation of extreme wind speeds. The extreme velocity components and horizontal wind speeds were evaluated based on the gust factor (GF) and peak factor (PF). The observations of this study are summarized below:

The spatial distributions of the GF and PF within the canopy were compared qualitatively using various statistics, namely, the mean wind speed, integral time scale, standard deviation, skewness (third-order moment), kurtosis (fourth-order moment), and fifth-order moment. Both GF and PF in the contraction regions of the flow by two blocks became

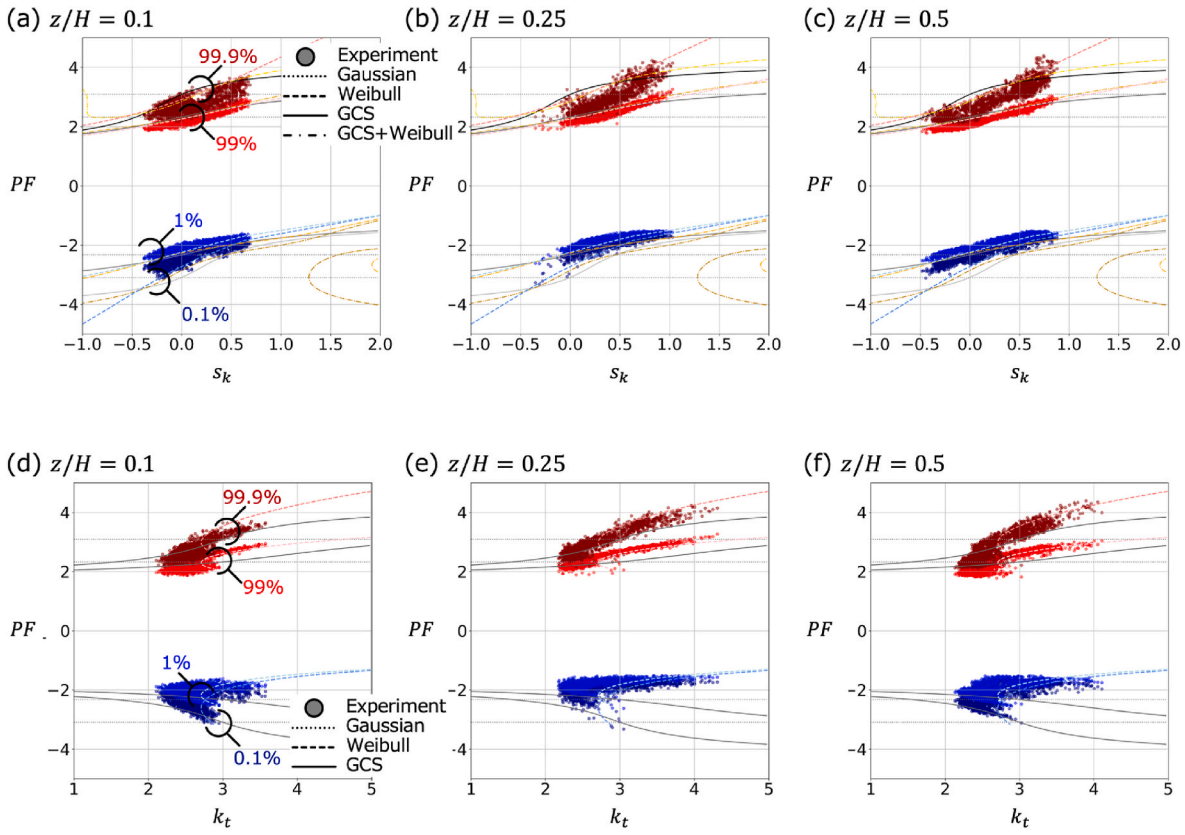

Fig. 13. Identical to Fig. 11 except for the wind speed v_a at the three heights (z/H) of (a,d) 0.1, (b,e) 0.25, and (c,f) 0.5. (a,b,c) Skewness s_k and (d,e,f) kurtosis k_t.

smaller than those of the surroundings. In addition, these regions exhibited smaller values of the high-order moment and integral time scale. These qualitative correlations between the rare wind speed and statistics indicate the importance of considering the spatial variations in PF and GF within the urban canopy area.

Accordingly, to understand the effect of the flow patterns within the canopy on the PDFs and PSDs, these were classified based on i) whether the streamwise flow was favorable or reverse and ii) whether the spanwise velocity component was dominant or not. This revealed that the PDFs of u were skewed marginally in the positive-flow regions, whereas those of v were sharpened when v dominated the flow direction. Unlike the variation in the PDFs based on the mean flow patterns, the differences in the PSD are unapparent in the present datasets.

To quantify the relationship between the statistics and PF or GF, the correlation coefficients between PF or GF and the various statistics (namely, the mean, standard deviation, third-to six-order moments, and integral time scale) were determined. Strong correlations were verified between GF and s_k, k_t., PF and s_k for wind speed PF and skewness. They were larger than 0.6. In contrast, the correlations between the PF and integral time scale τ were relatively weak and less than 0.4 probably because we considered the overall correlations in the three unit planes at the three heights. Therefore, further investigations based on different types of turbulent flow at the pedestrian level are required for the correlations between PF and τ.

Based on the observations of the strong correlations between PF, s_k, and k_t, the relationship between s_k or k_t and PF was compared with the prediction by statistical methods based on three distribution functions: Gaussian, Weibull, and GCS. Both strong and weak velocity components and the wind speed showed clusters around the prediction using statistical methods. The agreement between the data and theoretical line was significant, particularly for the wind speed v_a, justifying that the probability density of the canopy wind speed can be modeled by the statistical models.

These observations clearly validate the previous statistical methods of Wang and Okaze [21,22], Wang et al. [23], and Seta et al. [24]. Therein, the extreme values were predicted using s_k ([21,22]), k_t, and higher-order moments ([23,24]). In addition, the present results signify that the influential factors on the PF or low-occurrence wind speeds are accumulated in these statistics. This also indicates that collecting high-order moments (or the nth-powered accumulation of a random variable) is consequential for predicting the PF, although the physical significance of these statistics is ambiguous. Notwithstanding the ambiguous physical interpretations of high-order moments, it would be useful to establish an inductive prediction model, such as a deep learning model. Another contribution to the research field is that we provide effective datasets of canopy flow owing to the development of the canopy measurement system by Hirose et al. [18]. The PIV datasets addressing the entire plane of the canopy enabled us to perform these statistical analyses.

It should be noted that only one array was used. It is well known that, as geometrical impact on the wind speed within the canopy, other geometrical conditions such as the height variation, packing density, street path length are required to verify whether these parameters can dramatically alter the PDFs and percentiles. Furthermore, the relationship between moments, GF, and PF should be accumulated to validate the statistical methods for various types of building cases and flow patterns. These aspects should also be considered in future studies.

Funding

This study was partially supported by a Grant-in-Aid for Scientific Research from JSPS KAKENHI (Grant No. JP23H01569), the FOREST program from JST (Grant No. JPMJFR205O), and the Initiative for Realizing Diversity in the Research Environment.

CRediT authorship contribution statement

Fei Li: Writing – original draft, Investigation, Formal analysis. **Chiyoko Hirose:** Methodology, Investigation. **Wei Wang:** Methodology, Investigation. **Chun-Ho Liu:** Writing – review & editing, Supervision. **Naoki Ikegaya:** Writing – review & editing, Writing – original draft, Supervision, Funding acquisition, Formal analysis.

Declaration of competing interest

The authors declare that they have no known competing financial interests or personal relationships that could have appeared to influence the work reported in this paper.

Data availability

Data will be made available on request.

Appendix 1. Convergence of statistics

It is well known that the higher order moments defined by Eq. (3.7) require a longer period for the convergence. In preliminary experiments, we have conducted three trials of the PIV following the procedures in Section 2.2 for the A1 at $z/H = 0.5$. Hence, the total data acquisition period is 30s. Figs. 14 and 15 show the variation ratio R and coefficient of variation CV of the wind speed v_a with respect to the sampling period T. R was defined the ratio between the statistics during T to those of $T = 30$ s. CV was calculated by the ratio between the standard deviation to mean values of the statistics defined by the randomly resampled 100 set of data during T.

Fig. 14 clearly shows that all the moments rapidly converge after approximately $T = 5$ s. At $T = 20$ s, which is the data acquisition period of this study, the values of R for $\overline{v_a}$ and σ_{v_a} are less than 5 %. Those of s_k, k_t, m_5, and m_6 are less than 10 %. As for m_7 and m_8, the values of R becomes larger than 10 %, and the data of m_9 and m_{10} are not included because they vary more than 100 %, indicating these higher order statistics are not converged in $T = 20$ s. In addition to the convergence of statistics, Fig. 15 shows the expected variations of the statistics in a sampling period T. The values of CV at $T = 20$ s of $\overline{v_a}$ and σ_{v_a} are less than 0.5 %, those of s_k and k_t are less than 4 %, and those of m_5 and m_6 are less approximately 5 %. CV of m_7 is larger, and m_8 reach to 0.35 even at $T = 20$ s.

According to these data, we reached following conclusions. The bias errors due to the data acquisition period for the mean and standard deviation were 5 %, those of s_k to m_6 were 10 %, and those of other higher-order statistics were larger. The variations of the determined values in each trial were approximately 0.5 % for the mean and standard deviation, and 5 % for s_k to m_6.

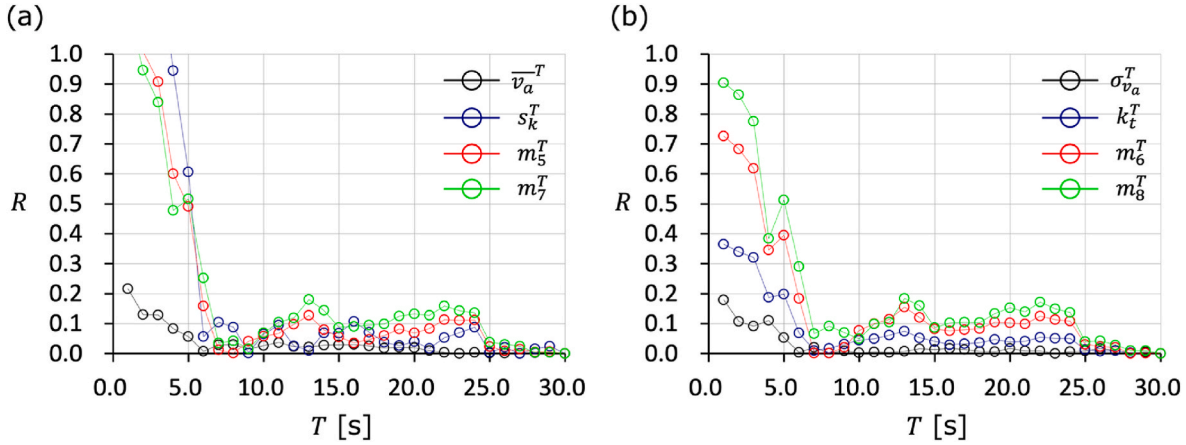

Fig. 14. The convergence of the statistic during a sampling period T [s] at $x/H = y/H = z/H = 0.5$ for the wind speed v_a. R indicates the ratio of the statistics determined in T and that of $T = 30$ s. The suffix T indicates the statistics dertermined in T. (a) Odd-order moments, and (b) even-order moments defined by Eq. (3.7).

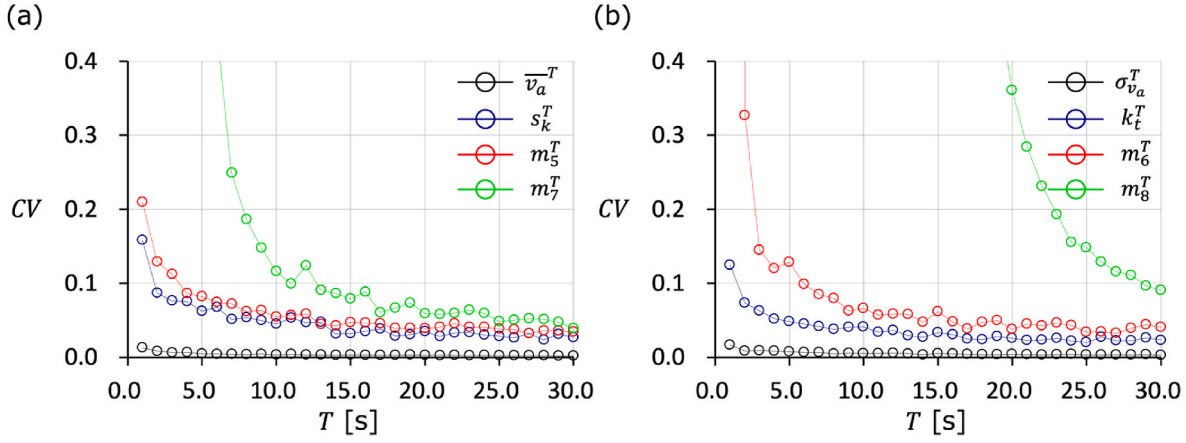

Fig. 15. The coefficient of varition, CV, of the statistics for a period T [s] for the wind speed v_a at $x/H = y/H = z/H = 0.5$. A dataset during T was randomly sampled from the whole data and a hundred datasets were used determine CV. (a) Odd-order moments, and (b) even-order moments defined by Eq. (3.7).

References

[1] B. Blocken, T. Stathopoulos, J.P.A.J. van Beeck, Pedestrian-level wind conditions around buildings: review of wind-tunnel and CFD techniques and their accuracy for wind comfort assessment, Build, Environ. Times 100 (2016) 50–81, https://doi.org/10.1016/j.buildenv.2016.02.004.

[2] E. Ng, Policies and technical guidelines for urban planning of high-density cities - air ventilation assessment (AVA) of Hong Kong, Build. Environ. 44 (2009) 1478–1488, https://doi.org/10.1016/j.buildenv.2008.06.013.

[3] C. Yuan, E. Ng, Building porosity for better urban ventilation in high-density cities - a computational parametric study, Build. Environ. 50 (2012) 176–189, https://doi.org/10.1016/j.buildenv.2011.10.023.

[4] T. Kubota, M. Miura, Y. Tominaga, A. Mochida, Wind tunnel tests on the relationship between building density and pedestrian-level wind velocity: development of guidelines for realizing acceptable wind environment in residential neighborhoods, Build, Environ. Times 43 (2008) 1699–1708, https://doi.org/10.1016/j.buildenv.2007.10.015.

[5] T. Hu, R. Yoshie, Indices to evaluate ventilation efficiency in newly-built urban area at pedestrian level, J. Wind Eng. Ind. Aerod. 112 (2013) 39–51, https://doi.org/10.1016/j.jweia.2012.11.002.

[6] A. Abd Razak, A. Hagishima, N. Ikegaya, J. Tanimoto, Analysis of airflow over building arrays for assessment of urban wind environment, Build. Environ. 59 (2013) 56–65, https://doi.org/10.1016/j.buildenv.2012.08.007.

[7] C. Yuan, L. Norford, R. Britter, E. Ng, A modelling-mapping approach for fine-scale assessment of pedestrian-level wind in high-density cities, Build. Environ. 97 (2016) 152–165, https://doi.org/10.1016/j.buildenv.2015.12.006.

[8] Y. He, Z. Liu, E. Ng, Parametrization of irregularity of urban morphologies for designing better pedestrian wind environment in high-density cities – a wind tunnel study, Build. Environ. 226 (2022), https://doi.org/10.1016/j.buildenv.2022.109692.

[9] N. Ikegaya, Y. Ikeda, A. Hagishima, A.A. Razak, J. Tanimoto, A prediction model for wind speed ratios at pedestrian level with simplified urban canopies, Theor. Appl. Climatol. 127 (2017) 655–665, https://doi.org/10.1007/s00704-015-1655-z.

[10] Y. Ishida, T. Okaze, A. Mochida, Influence of urban configuration on the structure of kinetic energy transport and the energy dissipation rate, J. Wind Eng. Ind. Aerod. 183 (2018) 198–213, https://doi.org/10.1016/j.jweia.2018.10.016.

[11] N. Ikegaya, T. Kawaminami, T. Okaze, A. Hagishima, Evaluation of exceeding wind speed at a pedestrian level around a 1:1:2 isolated block model, J. Wind Eng. Ind. Aerod. 201 (2020), 104193, https://doi.org/10.1016/j.jweia.2020.104193.

[12] N. Ikegaya, Y. Ikeda, A. Hagishima, J. Tanimoto, Evaluation of rare velocity at a pedestrian level due to turbulence in a neutrally stable shear flow over simplified urban arrays, J. Wind Eng. Ind. Aerod. 171 (2017) 137–147, https://doi.org/10.1016/j.jweia.2017.10.002.

[13] T. Kawaminami, N. Ikegaya, A. Hagishima, J. Tanimoto, Velocity and scalar concentrations with low occurrence frequencies within urban canopy regions in a neutrally stable shear flow over simplified urban arrays, J. Wind Eng. Ind. Aerod. 182 (2018) 286–294, https://doi.org/10.1016/j.jweia.2018.09.024.

[14] D. Hertwig, G. Patnaik, B. Leitl, LES validation of urban flow, part I: flow statistics and frequency distributions, Environ. Fluid Mech. 17 (2017) 521–550, https://doi.org/10.1007/s10652-016-9507-7.

[15] Y. Tominaga, M. Shirzadi, Wind tunnel measurement of three-dimensional turbulent flow structures around a building group: impact of high-rise buildings on pedestrian wind environment, Build. Environ. 206 (2021), 108389, https://doi.org/10.1016/j.buildenv.2021.108389.

[16] Y. Tominaga, M. Shirzadi, Wind tunnel measurement dataset of 3D turbulent flow around a group of generic buildings with and without a high-rise building, Data Brief 39 (2021), 107504, https://doi.org/10.1016/j.dib.2021.107504.

[17] Y.M. H'ng, N. Ikegaya, S.A. Zaki, A. Hagishima, A.F. Mohammad, Wind-tunnel estimation of mean and turbulent wind speeds within canopy layer for urban campus, Urban Clim. 41 (2022), 101064, https://doi.org/10.1016/j.uclim.2021.101064.

[18] C. Hirose, T. Nomichi, N. Ikegaya, Distributions of gust and peak factors at a pedestrian level in a simplified urban canopy obtained by particle image velocimetry, Build. Environ. 109350 (2022), https://doi.org/10.1016/j.buildenv.2022.109350.

[19] I.C. Tolias, N. Koutsourakis, D. Hertwig, G.C. Efthimiou, A.G. Venetsanos, J. G. Bartzis, Large Eddy Simulation study on structure of turbulent flow in a complex city, J. Wind Eng. Ind. Aerod. 177 (2023) (2018) 101–116, https://doi.org/10.1016/j.jweia.2018.03.017.

[20] G.C. Efthimiou, D. Hertwig, S. Andronopoulos, J.G. Bartzis, O. Coceal, A statistical model for the prediction of wind-speed probabilities in the atmospheric surface layer, Boundary-Layer Meteorol. 163 (2017) 179–201, https://doi.org/10.1007/s10546-016-0221-2.

[21] W. Wang, T. Okaze, Statistical analysis of low-occurrence strong wind speeds at the pedestrian level around a simplified building based on the Weibull distribution, Build. Environ. 209 (2022), 108644, https://doi.org/10.1016/j.buildenv.2021.108644.

[22] W. Wang, T. Okaze, Estimating low-occurrence wind speeds from mean velocity and turbulent kinetic energy: development of statistical method and validation with idealized cases, Build. Environ. 224 (2022), 109499, https://doi.org/10.1016/j.buildenv.2022.109499.

[23] W. Wang, K. Seta, N. Ikegaya, Modelling probability density functions based on the Gram–Charlier series with higher-order statistics: theoretical derivation and application, J. Wind Eng. Ind. Aerod. 231 (2022), 105227, https://doi.org/10.1016/j.jweia.2022.105227.

[24] K. Seta, W. Wang, N. Ikegaya, Modeling probability density functions of instantaneous velocity components at the pedestrian levels of a building array by Gram–Charlier series, J. Wind Eng. Ind. Aerod. 239 (2023), 105427, https://doi.org/10.1016/j.jweia.2023.105427.

[25] A. Hald, The early history of the cumulants and the Gram-Charlier series, Int. Stat. Rev. 68 (2000) 137–153, https://doi.org/10.1111/j.1751-5823.2000.tb00318.x.

[26] W. Wang, N. Ikegaya, T. Okaze, Comparing Weibull distribution method and Gram–Charlier series method within the context of estimating low-occurrence strong wind speed of idealized building cases, J. Wind Eng. Ind. Aerod. 236 (2023), 105401, https://doi.org/10.1016/j.jweia.2023.105401.

[27] M.A. bin Zainol, N. Ikegaya, M.F. Mohamad, Stochastic and statistical characteristics of artificially generated turbulent flow following karman spectrum in a wind-tunnel experiment, J. Wind Eng. Ind. Aerod. 229 (2022), 105148, https://doi.org/10.1016/j.jweia.2022.105148.

[28] N. Ikegaya, S. Hasegawa, A. Hagishima, Time-resolved particle image velocimetry for cross-ventilation flow of generic block sheltered by urban-like block arrays, Build. Environ. 147 (2019) 132–145, https://doi.org/10.1016/j.buildenv.2018.10.015.

[29] A. Hagishima, J. Tanimoto, K. Nagayama, S. Meno, Aerodynamic parameters of regular arrays of rectangular blocks with various geometries, Boundary-Layer Meteorol. 132 (2009) 315–337, https://doi.org/10.1007/s10546-009-9403-5.

[30] W.H. Snyder, I.P. Castro, The critical Reynolds number for rough-wall boundary layers, J. Wind Eng. Ind. Aerod. 90 (2002) 41–54, https://doi.org/10.1016/S0167-6105(01)00114-3.

[31] K. Uehara, S. Wakamatsu, R. Ooka, Studies on critical Reynolds number indices for wind-tunnel experiments on flow within urban areas, Boundary-Layer Meteorol. 107 (2003) 353–370, https://doi.org/10.1023/A:1022162807729.

[32] O. Coceal, T.G. Thomas, I.P. Castro, S.E. Belcher, Mean flow and turbulence statistics over groups of urban-like cubical obstacles, Boundary-Layer Meteorol. 121 (2006) 491–519, https://doi.org/10.1007/s10546-006-9076-2.

[33] O. Coceal, A. Dobre, T.G. Thomas, S.E. Belcher, Structure of turbulent flow over regular arrays of cubical roughness, J. Fluid Mech. 589 (2007) 375–409, https://doi.org/10.1017/S002211200700794X.

[34] O. Coceal, T.G. Thomas, S.E. Belcher, Spatial variability of flow statistics within regular building arrays, Boundary-Layer Meteorol. 125 (2007) 537–552, https://doi.org/10.1007/s10546-007-9206-5.

[35] Z. Xie, I.P. Castro, LES and RANS for turbulent flow over arrays of wall-mounted obstacles, Flow, Turbul. Combust. 76 (2006) 291–312, https://doi.org/10.1007/s10494-006-9018-6.

[36] S. Herpin, L. Perret, R. Mathis, C. Tanguy, J. Lasserre, Investigation of the flow inside an urban canopy immersed into an atmospheric boundary layer using laser Doppler anemometry, Exp. Fluid 59 (2018) 80.

[37] T. von Karman, Progress in the statistical theory of turbulence, Proc. N. A. S. 34 (1948) 530–539.

[38] J. Kaima, J.C. Wyngaard, Y. Izumi, O.R. Cote, Spectral characteristics of surface-layer turbulence, Auart. J. R. Met Soc. (1972) 563–589.

[39] J. Maeda, M. Makino, Characteristics of gusty winds simulated by an ARMA model, J. Wind Eng. Ind. Aerod. 41–44 (1992) 427–436.

[40] C. Hirose, N. Ikegaya, A. Hagishima, Outdoor measurements of relationship between canopy flow and wall pressure distributions of a block within urban-like block array, Build. Environ. 176 (2020), 106881, https://doi.org/10.1016/j.buildenv.2020.106881.

[41] M. Kanda, Large-eddy simulations on the effects of surface geometry of building arrays on turbulent organized structures, Boundary-Layer Meteorol. 118 (2006) 151–168, https://doi.org/10.1007/s10546-005-5294-2.

[42] J.J. Finnigan, R.H. Shaw, E.G. Patton, Turbulence structure above a vegetation canopy, J. Fluid Mech. 637 (2009) 387–424, https://doi.org/10.1017/S0022112009990589.

[43] M.R. Raupach, Conditional statistics of Reynolds stress in rough-wall and smooth-wall turbulent boundary layers, J. Fluid Mech. 108 (1981) 363–382, https://doi.org/10.1017/S0022112081002164.

[44] J. Finnigan, Turbulence in plant canopies, Annu. Rev. Fluid Mech. 32 (2000) 519–571.

[45] T. Michioka, H. Takimoto, H. Ono, A. Sato, Effects of fetch on turbulent flow and pollutant dispersion within a cubical canopy, Boundary-Layer Meteorol. 168 (2018) 247–267, https://doi.org/10.1007/s10546-018-0339-5.

[46] H. Rinne, The Weibull Distribution: a Hand Book, CRC press, 2008.